iScience

CellPress
OPEN ACCESS

Article

Multi-omics-based label-free metabolic flux inference reveals obesity-associated dysregulatory mechanisms in liver glucose metabolism

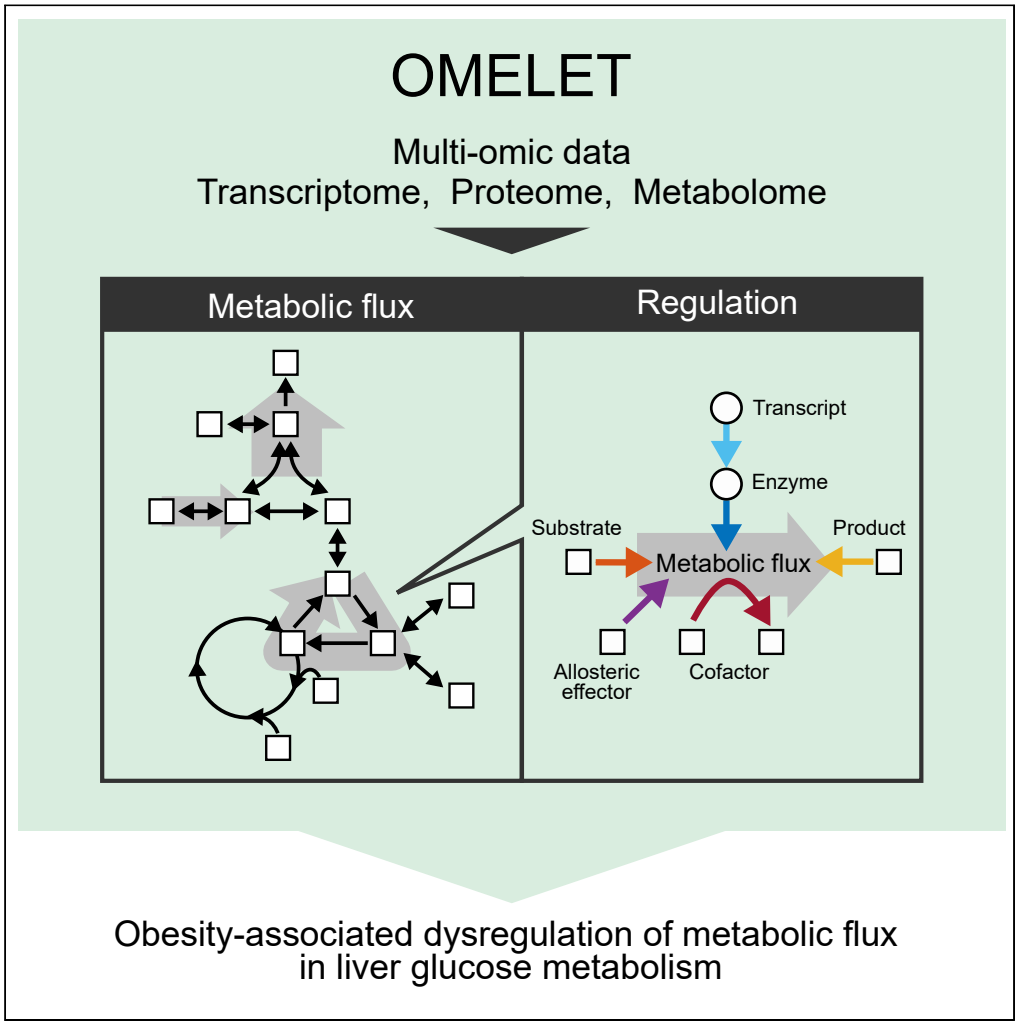

Saori Uematsu, Satoshi Ohno, Kaori Y. Tanaka, ..., Akiyoshi Hirayama, Tomoyoshi Soga, Shinya Kuroda

s-ohno@bs.s.u-tokyo.ac.jp (S.O.)
skuroda@bs.s.u-tokyo.ac.jp (S.K.)

Highlights

We developed OMELET to infer metabolic flux from label-free multi-omic data

Contributions of metabolites, enzymes, and transcripts for flux were inferred

Gluconeogenic flux increased in fasting *ob*/*ob* mice by increased transcripts

Increased pyruvate cycle fluxes were led by increased transcripts and substrates

Uematsu et al., iScience *25*, 103787
February 18, 2022
https://doi.org/10.1016/j.isci.2022.103787

iScience

CellPress
OPEN ACCESS

Article

Multi-omics-based label-free metabolic flux inference reveals obesity-associated dysregulatory mechanisms in liver glucose metabolism

Saori Uematsu,[1] Satoshi Ohno,[2,3,*] Kaori Y. Tanaka,[1] Atsushi Hatano,[4] Toshiya Kokaji,[3] Yuki Ito,[1,5] Hiroyuki Kubota,[5] Ken-ichi Hironaka,[3] Yutaka Suzuki,[1] Masaki Matsumoto,[4] Keiichi I. Nakayama,[6] Akiyoshi Hirayama,[7] Tomoyoshi Soga,[7] and Shinya Kuroda[1,2,3,8,*]

SUMMARY

Glucose homeostasis is maintained by modulation of metabolic flux. Enzymes and metabolites regulate the involved metabolic pathways. Dysregulation of glucose homeostasis is a pathological event in obesity. Analyzing metabolic pathways and the mechanisms contributing to obesity-associated dysregulation *in vivo* is challenging. Here, we introduce OMELET: Omics-Based Metabolic Flux Estimation without Labeling for Extended *Trans*-omic Analysis. OMELET uses metabolomic, proteomic, and transcriptomic data to identify relative changes in metabolic flux, and to calculate contributions of metabolites, enzymes, and transcripts to the changes in metabolic flux. By evaluating the livers of fasting *ob/ob* mice, we found that increased metabolic flux through gluconeogenesis resulted primarily from increased transcripts, whereas that through the pyruvate cycle resulted from both increased transcripts and changes in substrates of metabolic enzymes. With OMELET, we identified mechanisms underlying the obesity-associated dysregulation of metabolic flux in the liver.

INTRODUCTION

Glucose homeostasis is tightly regulated to meet the energy requirements of vital organs and maintain health. Dysregulation of glucose homeostasis leads to metabolic diseases such as obesity and type 2 diabetes (Hotamisligil and Erbay, 2008; Kahn et al., 2006; Petersen et al., 2017). The liver plays a central role in glucose homeostasis by regulating various pathways of glucose metabolism, including gluconeogenesis and glycolysis (Han et al., 2016; Nordlie et al., 1999; Petersen et al., 2017). The liver is a major player in the pathophysiology of obesity (Charlton, 2004; Polyzos et al., 2019; Roden and Shulman, 2019). Fasting hyperglycemia in obesity is attributed to altered glucose metabolism in the liver because of insulin resistance. Because of the complex nature of the obesity-associated pathophysiology of glucose metabolism in the liver, investigation of the dysregulation in this metabolic system requires data of multiple types that are obtained under the same condition.

Metabolic flux, the rate of turnover of molecules through a metabolic reaction, is a direct measure of the activity of the reaction (Jang et al., 2018). Metabolic flux through a reaction is regulated by multiple molecules: enzymes, substrates, products, and cofactors. Enzymes are regulated by allosteric effectors and other factors such as posttranslational modifications of enzymes. The amounts of enzymes are determined by the amounts of transcripts encoding the corresponding enzymes and other factors such as translation and protein degradation. To investigate metabolic flux and its complex regulation, the amounts of all the regulators of metabolic flux should be simultaneously measured because molecular interactions between metabolome layer and other multiple omic layers are mutually connected (Wiley, 2011; Yugi et al., 2014). The amounts of enzymes can be measured by mass spectrometry-based proteomics, transcripts for enzymes by RNA sequencing, and the amounts of substrates, products, cofactors, and allosteric effectors by mass spectrometry-based metabolomics. We developed a method of *trans*-omic analysis based on direct molecular interactions to construct a multilayered biochemical network using simultaneously obtained multi-omic data (Egami et al., 2021; Kawata et al., 2018; Kokaji et al., 2020; Yugi et al., 2014, 2016). The *trans*-omic analysis investigated the regulation of metabolic reactions from changes in

[1]Department of Computational Biology and Medical Sciences, Graduate School of Frontier Sciences, The University of Tokyo, 5-1-5 Kashiwanoha, Kashiwa, Chiba 277-8562, Japan

[2]Molecular Genetic Research Laboratory, Graduate School of Science, The University of Tokyo, 7-3-1 Hongo, Bunkyo-ku, Tokyo, Japan

[3]Department of Biological Sciences, Graduate School of Science, The University of Tokyo, 7-3-1 Hongo, Bunkyo-ku, Tokyo 113-0033, Japan

[4]Department of Omics and Systems Biology, Graduate School of Medical and Dental Sciences, Niigata University, 757 Ichibancho, Asahimachi-dori, Chuo-ku, Niigata City, Niigata 951-8510, Japan

[5]Division of Integrated Omics, Research Center for Transomics Medicine, Medical Institute of Bioregulation, Kyushu University, 3-1-1 Maidashi, Higashi-ku, Fukuoka 812-8582, Japan

[6]Department of Molecular and Cellular Biology, Medical Institute of Bioregulation, Kyushu University, 3-1-1 Maidashi, Higashi-ku, Fukuoka 812-8582, Japan

[7]Institute for Advanced Biosciences, Keio University, 246-2 Mizukami, Kakuganji, Tsuruoka, Yamagata 997-0052, Japan

[8]Lead contact

*Correspondence: s-ohno@bs.s.u-tokyo.ac.jp (S.O.), skuroda@bs.s.u-tokyo.ac.jp (S.K.)

https://doi.org/10.1016/j.isci.2022.103787

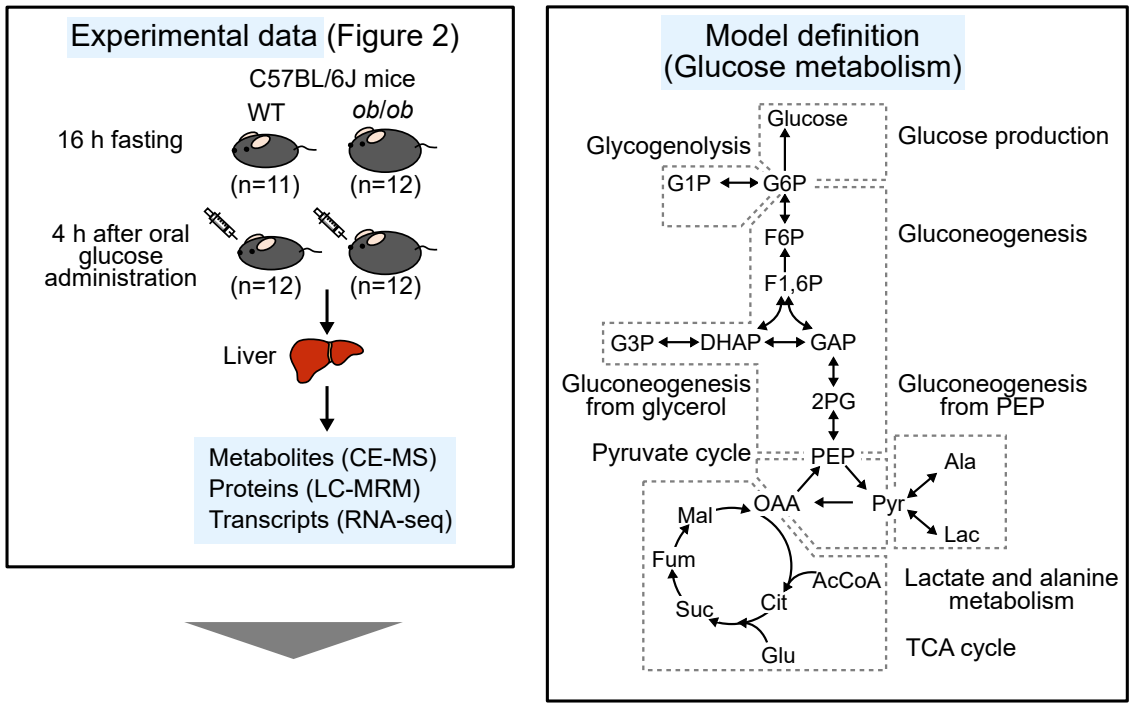

Step 1: Infer metabolic flux and identify changes in metabolic flux between conditions (Figures 3 and 4)

Input: Experimental data, Model definition → OMELET → Output: Metabolic flux, Kinetic parameters

Step 2: Quantify contributions of regulators to changes in metabolic flux (Figures 5, 7A, and 7B)

Input: Experimental data + Kinetic parameters → Output: Contribution

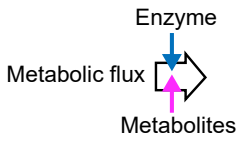

Step 3: Construct a quantitaive trans-omic network for changes in metabolic flux (Figures 6 and 7C)

Input: Experimental data + Metabolic flux (Step 1) + Contribution (Step 2) → Output: Quantitative trans-omic network

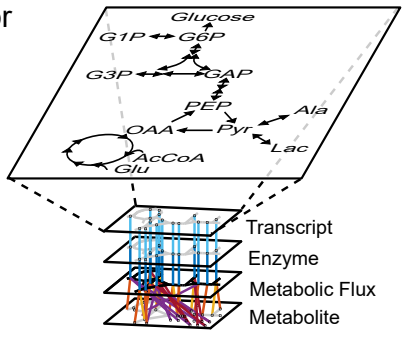

Please cite this article in press as: Uematsu et al., Multi-omics-based label-free metabolic flux inference reveals obesity-associated dysregulatory mechanisms in liver glucose metabolism, iScience (2022), https://doi.org/10.1016/j.isci.2022.103787

Figure 1. Overview of the application of OMELET to study glucose metabolism

(Top right) Overview of glucose metabolism (see Table S1 for definitions of metabolites). The model definition is a simplified metabolic network and not the exact one used as inputs of OMELET. (Top left) Experimental data are acquired from livers of WT and *ob*/*ob* mice under fasting conditions and after oral glucose administration. These data serve as the input for Step 1.

molecule amounts in response to some perturbations or between conditions. This analysis generates genome-scale qualitative *trans*-omic networks, but does not directly indicate quantitative metabolic fluxes or how much each regulatory mechanism affects cellular metabolism. To incorporate the quantitative information on metabolic flux, isotopic labeling has been required.

The standard method for measuring metabolic flux is isotopic labeling, in which isotopic tracers are introduced into cells or living animals (Hasenour et al., 2015, 2020; Hiller and Metallo, 2013; Quek et al., 2010). To analyze the regulation of metabolic flux in a nonsteady state, we developed a kinetic *trans*-omic analysis that uses data from isotopic labeling experiments and inferred metabolic flux together with contributions of regulators to changes in metabolic flux across a multi-layered network (Ohno et al., 2020). Isotopic labeling is a powerful technique to measure metabolic flux, but it requires significant optimization to determine the appropriate isotopic tracers, their dosages, and the time course of isotopic enrichment of metabolites (Antoniewicz, 2018; Reisz and D'Alessandro, 2017). Recently multi-omic data including metabolomic, proteomic, and transcriptomic data have been increasingly obtained from various tissues and physiological conditions. Such multi-omic data would contain information on metabolic flux even without isotopic labeling. A mechanistic kinetic model is a promising method to integrate multi-omic data for quantitative understanding of metabolic fluxes and their regulations (Saa and Nielsen, 2017). However, most existing kinetic modeling frameworks require measured metabolic fluxes as inputs, and quantitative integration of several omic layers into one mathematical framework is still challenging. Therefore, developing methods to infer metabolic fluxes and their regulations from the multi-omic data without use of isotopic labeling is useful for investigation of dysregulation in the metabolic system such as obesity.

Here, we present a method that we termed Omics-Based Metabolic Flux Estimation without Labeling for Extended *Trans*-omic Analysis (OMELET). OMELET (i) infers metabolic fluxes in each condition from metabolomic, proteomic, and transcriptomic data, which are simultaneously obtained from the same individual samples, (ii) identifies relative changes in metabolic flux between the conditions, and (iii) calculates contributions of regulators to the changes in metabolic flux. We obtained metabolomic, proteomic, and transcriptomic data from the livers of wild-type (WT) and leptin-deficient obese (*ob*/*ob*) mice in the fasting state and 4 h after oral glucose administration. By applying OMELET to the experimental data, we inferred metabolic fluxes in each condition, and calculated contributions of regulators to changes in metabolic flux between the conditions. In the fasting state, metabolic fluxes through reactions in gluconeogenesis and the pyruvate cycle increased in *ob*/*ob* mice compared to WT mice. The increased metabolic fluxes through reactions in gluconeogenesis were caused by increased transcripts. In contrast, in the pyruvate cycle, the increased metabolic fluxes through pyruvate kinase (PK) involved increased transcripts and that through phosphoenolpyruvate carboxykinase (PEPCK) was caused by increased substrates. We also calculated the contributions of regulators to changes in metabolic flux resulting from oral glucose administration. In response to oral glucose administration, although the metabolic flux through PK did not change in both WT and *ob*/*ob* mice, the regulation of metabolic flux changed: PK flux was regulated by increased ATP as an allosteric inhibitor in WT mice, and by decreased PK-encoding transcript in *ob*/*ob* mice. Thus, OMELET provided quantitative mechanistic insights into obesity-associated differences in metabolic regulation in the liver without using isotopic tracers.

RESULTS

Overview of the application of OMELET to study glucose metabolism

In this study, we developed OMELET to infer metabolic flux using multi-omic data without using isotopic tracers, identify relative changes in metabolic flux between conditions, and calculate contributions of regulators to the changes in metabolic flux (Figure 1). We applied this method to evaluate the differences in metabolic flux in liver between WT and *ob*/*ob* mice, and the dysregulatory mechanisms associated with obesity. Additionally, we evaluated the differences in metabolic flux between the fasting state and 4-h after oral glucose administration for both WT mice and *ob*/*ob* mice. We had four conditions: WT in the fasting state, WT after oral glucose administration, *ob*/*ob* in the fasting state, and *ob*/*ob* after oral glucose administration. In each condition, we measured the amounts of metabolites, enzymes, and transcripts in liver

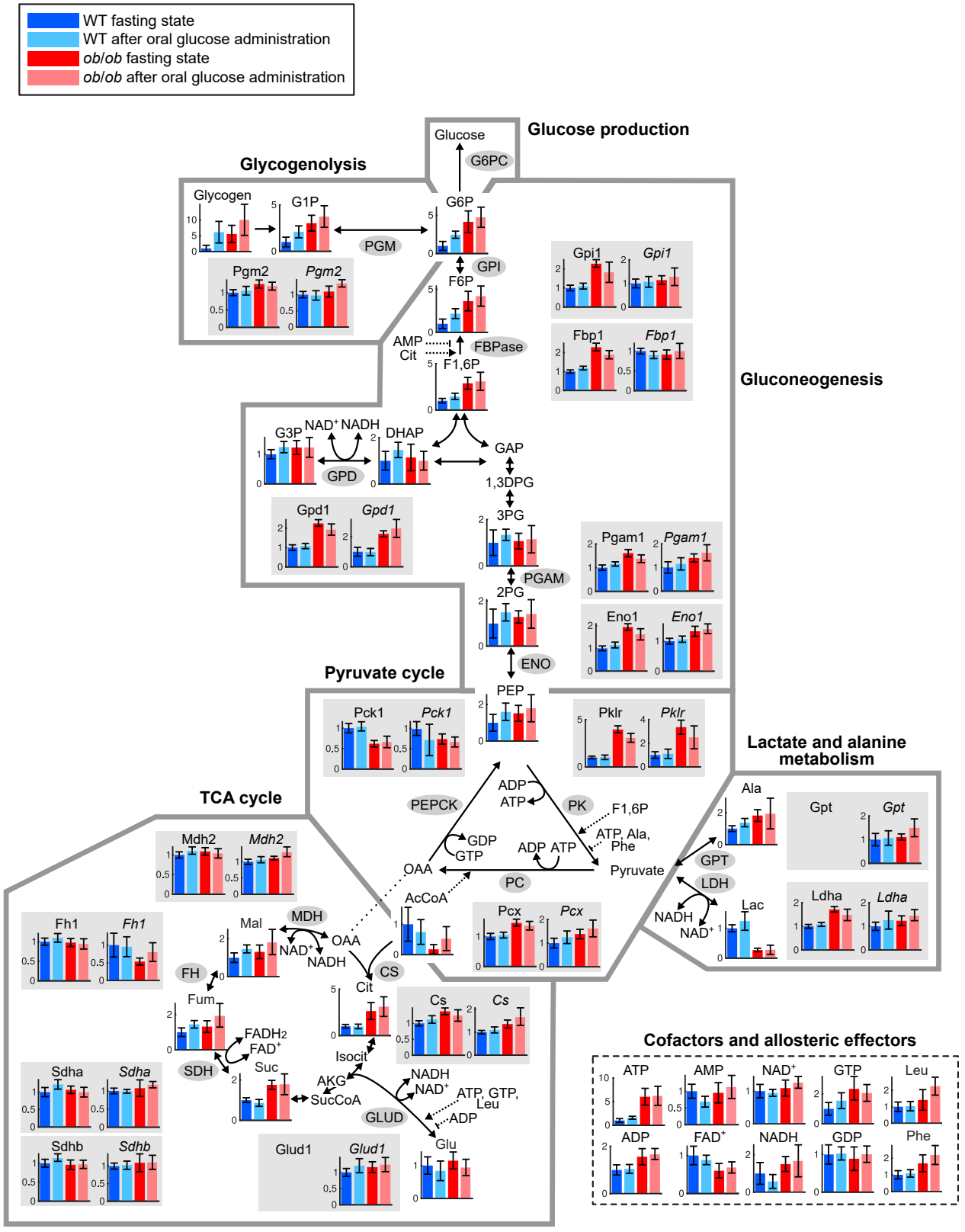
WT fasting state
WT after oral glucose administration
ob/ob fasting state
ob/ob after oral glucose administration
Glucose production
Glucose
G6PC
Glycogenolysis
Glycogen
G1P
PGM
G6P
GPI
F6P
Pgm2
Pgm2
Gpi1
Gpi1
AMP
Cit
FBPase
F1,6P
Fbp1
Fbp1
Gluconeogenesis
G3P
NAD+ NADH
GPD
DHAP
GAP
1,3DPG
Gpd1
Gpd1
3PG
Pgam1
Pgam1
PGAM
2PG
Eno1
Eno1
ENO
Pyruvate cycle
PEP
Pck1
Pck1
Pklr
Pklr
Lactate and alanine metabolism
TCA cycle
ADP
ATP
PEPCK
PK
F1,6P
GDP
GTP
ATP, Ala, Phe
ADP ATP
OAA
Pyruvate
PC
Ala
Gpt
Gpt
GPT
LDH
AcCoA
Pcx
Pcx
NADH
NAD+
Lac
Ldha
Ldha
Mdh2
Mdh2
Fh1
Fh1
Mal
MDH
OAA
NAD+
NADH
FH
CS
Cit
Fum
Cs
Cs
FADH2
FAD+
SDH
Isocit
Suc
AKG
SucCoA
NADH
NAD+
ATP, GTP, Leu
ADP
GLUD
Glu
Sdha
Sdha
Sdhb
Sdhb
Glud1
Glud1
Cofactors and allosteric effectors
ATP
AMP
NAD+
GTP
Leu
ADP
FAD+
NADH
GDP
Phe

Figure 2. Metabolomic, proteomic, and transcriptomic analysis of glucose metabolism in livers from WT and *ob*/*ob* mice in the fasting state and after oral glucose administration

Measured molecules (metabolites, enzymes, and transcripts) mapped onto the glucose metabolism in the liver. Only the metabolites, enzymes, and transcripts used in OMELET to evaluate the likelihood of the amounts of enzymes and transcripts are shown. Irreversible reactions are shown with one-headed arrows; reversible reactions are shown with double-headed arrows. Allosteric activation and inhibition are shown with dotted one-headed and dotted bar-headed arrows, respectively. The bars and error bars in each molecule represent the mean ± SD normalized to the mean of the data from WT in the fasting state. Enzymes and transcript results are shaded in gray. G6pc was measured at the transcript level but not at the protein level; Gpt and Glud1 were not measured at the protein level. Definitions of the metabolites, enzymes, and transcripts are described in Table S2.

samples from each mouse. We orally administered glucose to mice that had fasted for 16 h and collected livers before and 4 h after oral glucose administration (Figure 1: Experimental data).

By applying OMELET to the experimental data, we inferred metabolic fluxes in the glucose metabolism in each condition, and identified relative changes in metabolic flux between the conditions (Figure 1: Step 1). We focused on reactions in the glucose metabolism and inferred metabolic fluxes through the reactions in glycogenolysis, gluconeogenesis, lactate and alanine metabolism, the pyruvate cycle, and the TCA cycle (Figure 1; Table S1).

The changes in metabolic fluxes between conditions are caused by the changes of regulators such as enzymes and metabolites. To investigate which regulators caused changes in metabolic flux between the conditions, we calculated the contributions of the regulators to changes in metabolic flux from experimental data and kinetic parameters obtained in Step 1 (Figure 1: Step 2).

By integrating changes in the experimental data, changes in metabolic flux (Figure 1: Step 1), and contributions of the regulators to the changes in metabolic flux between the conditions (Figure 1: Step 2), we constructed a quantitative *trans*-omic network of the glucose metabolism in liver, which represents relative changes in metabolic flux and the regulation across multi-omic layers associated with obesity (Figure 1: Step 3).

Metabolomic, proteomic, and transcriptomic analysis of glucose metabolism in livers from WT and *ob*/*ob* mice in the fasting state and after oral glucose administration

We obtained metabolomic, proteomic, and transcriptomic data from livers of WT and *ob*/*ob* mice in the fasting state and 4 h after oral glucose administration. The dynamics of blood glucose and insulin concentrations differed between WT and *ob*/*ob* mice, consistent with obesity phenotype of the *ob*/*ob* mice (Figures S1A and S1B). However, both groups reached a steady state 4 h after oral glucose administration. The transcriptomic data were reported in our previous studies (Egami et al., 2021; Kokaji et al., 2020), and the metabolomic and proteomic data were obtained in this study (STAR Methods). We selected 28 metabolites, 15 enzymes, and 17 transcripts relevant to glucose metabolism from the metabolomic, proteomic, and transcriptomic data, respectively (Figure 2; Table S2). We defined transcript, enzyme, and reaction names as follows; transcript names are italicized with only the first letter in uppercase (*e.g.*, *Pklr*), enzyme names are not italicized with only the first letter in uppercase (*e.g.*, Pklr), and reaction names are not italicized with all letters in uppercase (*e.g.*, PK). Principal component analysis of the metabolites, enzymes, and transcripts showed that the first principal components captured differences between WT and *ob*/*ob* mice, and the second principal components captured changes by oral glucose administration (Figure S1C). The principal component analysis indicated that the differences between the genotypes, represented by principal component 1, exceeded the differences within the genotypes related to oral glucose administration, represented by principal component 2. Indeed, the principal component 1 represented $\geq$50% of the variance (58% for metabolites, 81% for enzymes, and 50% for transcripts) and principal component 2 represented $\leq$15% of the variance (11% for metabolites, 8% for enzymes, and 15% for transcripts).

We compared amounts of molecules between the conditions and defined increased and decreased molecules between the conditions. Molecules that showed an FDR-adjusted p value (q value) less than 0.05 were defined as significantly changed molecules. Among them, molecules that showed a fold change larger than 1.5 and smaller than 0.67 between the conditions were defined as increased and decreased molecules, respectively (Tables S2 and S3).

Consistent with the greatest separation between the genotypes by principal component analyses, we observed the greatest number of molecules in glucose metabolism differed between WT and *ob*/*ob*

mice (Tables S2 and S3). Comparing WT and *ob*/*ob* mouse livers in the fasting state showed that increased metabolites and enzymes in *ob*/*ob* mice included those in glycogenolysis and gluconeogenesis. After oral glucose administration, differences in metabolites in *ob*/*ob* mouse livers compared to WT mouse livers partially overlapped with the differences between the genotypes in the fasting state; however, only three increased enzymes were observed. WT mouse livers showed increases in metabolites of glycogenolysis and gluconeogenesis following glucose administration. In *ob*/*ob* mouse livers, no metabolites in glucose metabolism were significantly changed by glucose administration. Neither WT nor *ob*/*ob* mice had any changes in enzymes or transcripts when livers from fasting mice were compared to livers from mice of the same genotype after oral glucose administration. Although we could not find studies obtaining multi-omic data 4 h after oral glucose administration, the changes in metabolites, enzymes, and transcripts in *ob*/*ob* mice in the fasting state were consistent with those detected in diet-induced obese mice (Soltis et al., 2017).

The amounts of metabolites, enzymes, and transcripts do not directly reflect metabolic flux and its regulation; however, these data contain information to infer metabolic flux and its regulation. Therefore, we developed a method to infer metabolic flux and its regulation using the metabolomic, proteomic, and transcriptomic data.

Inference of metabolic fluxes by OMELET

OMELET is a probability-based model that incorporates metabolomic, proteomic, and transcriptomic data and uses kinetic equations to predict the parameters of metabolic flux, the elasticity coefficients, and the mRNA-to-protein ratios for each reaction (Figure 3). The advantages of OMELET are that metabolic flux can be inferred without using isotopic tracers, and that the regulation of metabolic flux can be determined from the kinetic parameters inferred by OMELET. The inputs of OMELET are the experimental data of the amounts of metabolites $\boldsymbol{x}$, enzymes $\boldsymbol{e}$, and transcripts $\boldsymbol{t}$ from the same mouse in each condition as well as model definitions, which are a stoichiometric matrix of the target metabolic pathway and information on cofactors and allosteric effectors for each reaction. The outputs are metabolic fluxes $\boldsymbol{v}$ in the target metabolic pathway in each condition, elasticity coefficients ε, and mRNA-to-protein ratios $\boldsymbol{\beta}$. The elasticity coefficient is the change in metabolic flux in response to infinitesimal changes in metabolites normalized to a reference condition. OMELET is based on a Bayesian method that calculates posterior probability of the output parameters $p(\boldsymbol{v}, \varepsilon, \boldsymbol{\beta}|\boldsymbol{x}, \boldsymbol{e}, \boldsymbol{t})$ by updating prior probability of parameters [$p(\boldsymbol{v}|\boldsymbol{u})$, $p(\varepsilon)$, and $p(\boldsymbol{\beta})$] and the hyperprior of independent flux $p(\boldsymbol{u}|\boldsymbol{\mu}^{u})$. The advantages of a Bayesian method are to avoid the problem of overfitting by defining appropriate priors and to assess parameter uncertainties by evaluating the posterior parameter distributions rather than the best optimal parameter values. The posterior probability of the output parameters is achieved by evaluating likelihoods $p(\boldsymbol{e}, \boldsymbol{t}|\boldsymbol{x}, \boldsymbol{v}, \boldsymbol{\beta}, \varepsilon)$ of the proteomic and transcriptomic data under a given metabolomic data and parameter set including metabolic flux (STAR Methods). Thus, the posterior probability reflects the experimental or biological noises of the measured data and to what extent the goodness of fit changes with altered parameter values. Metabolic flux $\boldsymbol{v}$ in a given metabolic pathway under a steady state condition can be written as a linear combination of independent flux $\boldsymbol{u}$, and the prior probability of metabolic flux $p(\boldsymbol{v}|\boldsymbol{u})$ is assumed to follow a multivariate normal distribution $\mathcal{N}(\boldsymbol{v}_l|\boldsymbol{\mu}_l^{v}, \boldsymbol{\Sigma}_l^{v})$. We used the elasticity coefficients ε and mRNA-to-protein ratios $\boldsymbol{\beta}$ to calculate the contributions of regulators to the changes in metabolic flux between the conditions. Thus, OMELET enabled identification of the specific reaction with relative changes in metabolic flux between the conditions and the extent to which specific regulators, such as changes in the amounts of enzymes and metabolites, contributed the inferred differences in metabolic flux between the conditions.

We validated the performance of OMELET by applying it to simulated datasets of the amounts of metabolites, enzymes, and metabolic fluxes in five conditions from kinetic models representing hepatocyte glucose metabolism (Marín-Hernández et al., 2020) and yeast glycolysis (Messiha et al., 2014; Smallbone et al., 2013) (Figure S2A; Table S4). The metabolic fluxes through most reactions inferred by OMELET highly correlated with those generated by steady state simulations of the kinetic models for different hepatocyte and yeast mutants (Figures S2B and S2C) except for those through reactions in glycogen metabolism of the hepatocyte kinetic model (Figure S2B). The fold changes of metabolic fluxes through reactions of the mutants over those of WT were almost consistent with those simulated by the hepatocyte or yeast kinetic model (Figures S2D and S2E). These results indicate that OMELET accurately identified the difference in metabolic fluxes across the reactions in each condition and the changes in metabolic flux among the

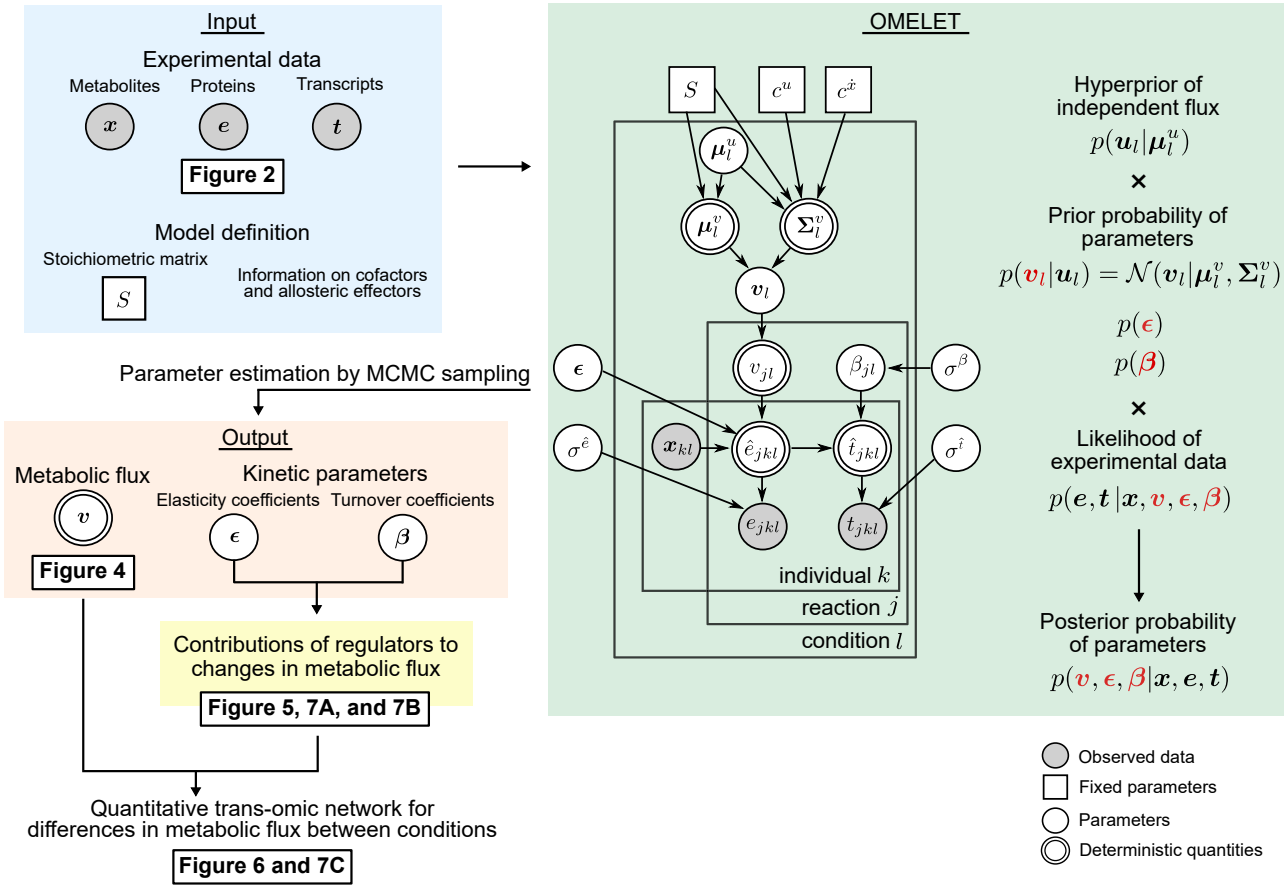

Figure 3. Inference of metabolic fluxes by OMELET

Overview of the workflow for the inference of metabolic flux. Shaded rectangles represent the inputs (light blue), OMELET (light green), the outputs (orange), and contributions (yellow). The inputs of OMELET were the experimental data of the amounts of metabolites $\boldsymbol{x}$, enzymes $\boldsymbol{e}$, and transcripts $\boldsymbol{t}$ from the same individual mice in each condition as well as model definitions including stoichiometric matrix and information on cofactors and allosteric effectors. The outputs were metabolic fluxes in the glucose metabolism $\boldsymbol{v}$ in each condition, elasticity coefficients $\boldsymbol{\epsilon}$, and mRNA-to-protein ratios $\boldsymbol{\beta}$. The output parameters are colored in red. In the graphical model, the plate indicates that the group-level structure holds for all the analyzed reactions $j \in R$, samples $k = 1,\ldots,n_l$, and conditions $l = 1,\ldots,g$. The arrows denote conditional dependencies between two nodes representing the generating processes (STAR methods). Shaded circles, unshaded squares, single-bordered circles, and double-bordered circles represent observed data, fixed parameters, parameters, and deterministic quantities, respectively. Using the kinetic parameters including elasticity coefficients and mRNA-to-protein ratios, we can calculate contributions of regulators to changes in metabolic flux between conditions.
See also STAR methods.

mutants. In addition, the validation using the hepatocyte and yeast kinetic models suggests that OMELET can be applied to different metabolic networks in different species.

Inference of metabolic fluxes in the glucose metabolism in liver of WT and *ob/ob* mice in the fasting state and after oral glucose administration

Because the blood glucose and insulin were constant both in WT and *ob/ob* mice in the fasting state and 4 h after oral glucose administration (Figures S1A and S1B) and the normalized rate of change in the amounts of metabolites and transcripts per hour approached zero around 4 h after oral glucose administration (Kokaji et al., 2020) (Figure S3), we assumed steady state conditions for glucose metabolism in livers of WT and *ob/ob* mice. By applying OMELET to the experimental data, we inferred metabolic fluxes in glucose metabolism in four conditions: WT and *ob/ob* mice in the fasting state and after oral glucose administration (Figures 4A and S4; Table S5). The posterior distributions of the metabolic fluxes were obtained by fitting the model to the experimental data for the amounts of enzymes and transcripts in each condition (Figure S5). We assumed that the liver produces glucose through gluconeogenesis, but does not consume glucose through glycolysis including glucokinase and phosphofructokinase, in all the

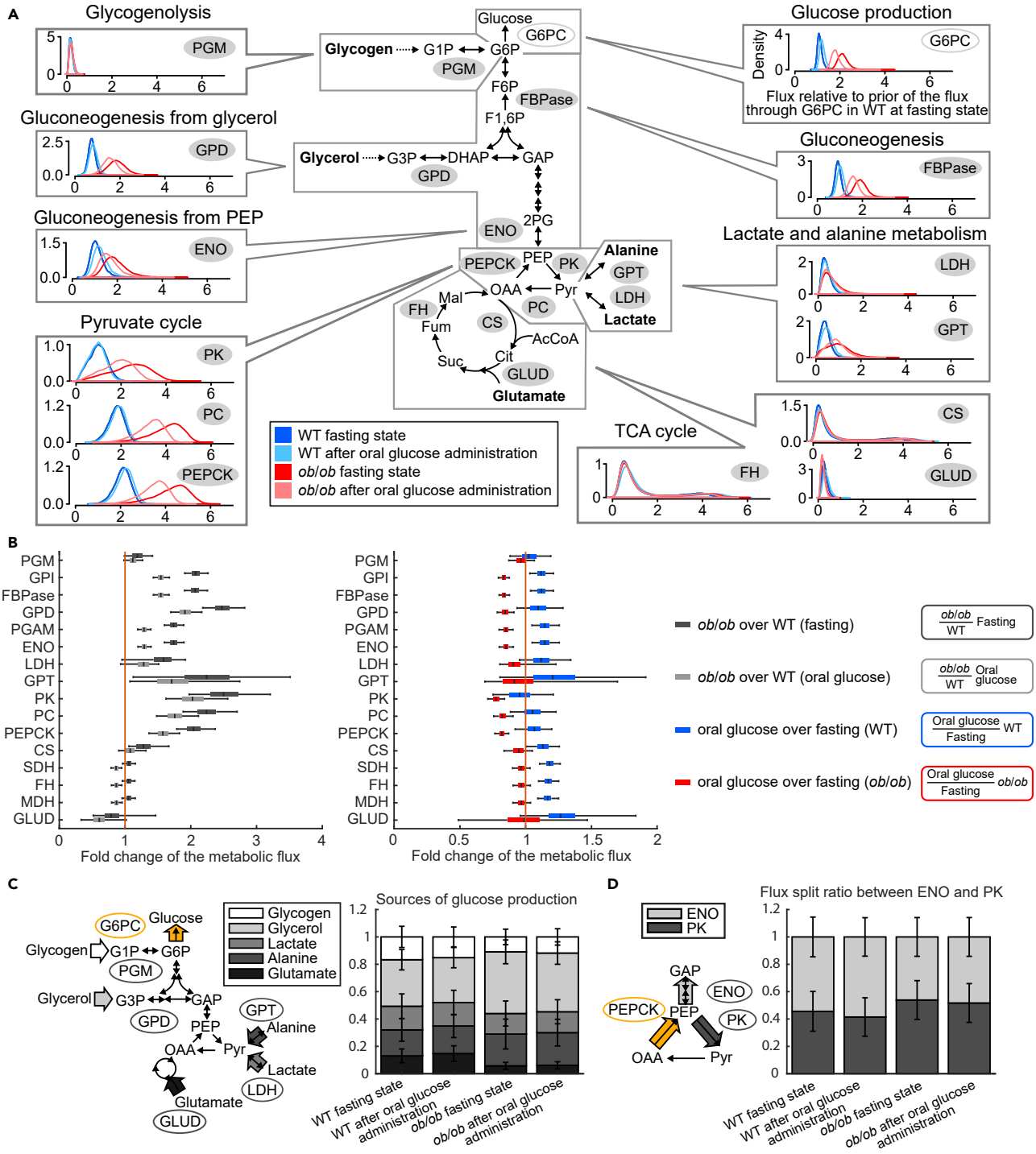

Figure 4. Inference of metabolic fluxes in the glucose metabolism in liver of WT and *ob/ob* mice in the fasting state and after oral glucose administration

(A) Posterior distributions of the metabolic fluxes in the glucose metabolism. Each box contains four density plots corresponding to four different conditions. Metabolic flux through each reaction is inferred relative to the mean of the prior for the metabolic flux through G6PC in WT mice in the fasting state. Only representative reactions (shaded gray circles in the map) in each pathway are presented See Figure S4 and Table S5 for complete reaction data

(B) Fold changes of the metabolic flux of *ob/ob* mice over that of WT mice in the fasting state (black bars) and after oral glucose administration (gray bars) in each reaction, and fold changes of the metabolic flux after oral glucose administration over that in the fasting state in WT mice (blue bars) and *ob/ob* mice (red bars) in each reaction. The median of the posterior distribution from OMELET is represented by a black line within the box for each reaction, the box

Figure 4. *Continued*

extends from the lower to the 25th and 75th percentiles, and the whiskers extend to 2.5th and 97.5th percentiles to cover 95% of the data. The vertical orange line indicates the boundary where a fold change equals one.

(C) Sources of glucose production. The stacked bars and error bars represent the mean ± SD of the proportions of glycogen, glycerol, lactate, alanine, and glutamate to the glucose production. The proportions of the sources are calculated from the proportion of metabolic fluxes through PGM, GPD, LDH, GPT, and GLUD, respectively (black circle), to that through G6PC (yellow circle).

(D) Flux split ratios between ENO and PK reactions. The stacked bars and error bars represent the mean ± SD of the proportions of the metabolic fluxes through ENO and PK to that through PEPCK.

conditions analyzed according to the previous studies (Jin et al., 2013; Turner et al., 2005). We fixed the direction of the reaction from glucose 6-phosphate (G6P) to glucose, mediated by glucose-6-phosphatase and indicated in the model as G6PC for glucose production. A metabolic flux through each reaction was simultaneously inferred in all the conditions as the relative value to that through G6PC in WT mice in the fasting state (STAR methods). Consequently, a total of 201 independent parameters were inferred by fitting the simulated amounts of 15 enzymes and 17 transcripts to the experimental data from 47 mice (1504 data points in total).

The metabolic flux through G6PC as glucose production is the sum of that through phosphoglucomutase (PGM) in glycogenolysis and fructose-1,6-bisphosphatase (FBPase) in gluconeogenesis. In WT mice in the fasting state, the 95% credible interval of the posterior distribution of the metabolic flux through FBPase (0.67–1.3) was not overlapped with that through PGM (0.05–0.38) (Figures 4A and S4; Table S5), suggesting that glucose production depended on gluconeogenesis. The small metabolic flux through PGM was consistent with the depletion of glycogen in WT mice in the fasting state (Figure 2). The metabolic flux through FBPase was further divided into that through glycerol-3-phosphate dehydrogenase (GPD) and alpha-enolase (ENO), which represented the metabolic flux through gluconeogenesis from glycerol and phosphoenolpyruvate (PEP), respectively. The metabolic flux through ENO (median of the posterior distribution: 1.1) and GPD (median: 0.75) were not significantly different (Figures 4A and S4; Table S5), indicating that both PEP and glycerol are equally used for glucose production. In the pyruvate cycle, the metabolic flux through PEPCK (median: 2.1) was larger than that through ENO (median: 1.1), and those through pyruvate carboxylase (PC) (median: 1.8) and PK (median: 0.98) were not significantly different from that through ENO (median: 1.1) (Figures 4A and S4; Table S5). This result suggested that PEP was equally used for glucose production and return to pyruvate. Although some studies showed that the inhibition of PK flux by glucagon prevents the futile pyruvate cycle in the fasting state (Large et al., 1997), the large metabolic flux though pyruvate cycle in the fasting state inferred by OMELET is consistent with that measured by the previous metabolic flux analysis in mice (Hasenour et al., 2015, 2020) and in rats (Beylot et al., 1995; Jones et al., 1997; Katz et al., 1993). The metabolic flux through PK (median: 0.98) was not significantly different from those through alanine aminotransferase (GPT) (median: 0.41) and lactate dehydrogenase (LDH) (median: 0.35), suggesting that pyruvate synthesis is equally contributed by the influxes from PEP, alanine, and lactate through PK, GPT, and LDH, respectively. In the TCA cycle, 95% credible intervals of the metabolic fluxes were large (0.21–4.1 on average) compared to those through other reactions in glucose metabolism (0.54–0.15 on average), indicating that the metabolic fluxes through reactions in the TCA cycle were not precisely determined. The metabolic fluxes in glucose metabolism in the liver of fasting WT mice inferred by OMELET were consistent with those by the previous metabolic flux analyses of fasting WT mice except for those in the TCA cycle (Burgess et al., 2015; Hasenour et al., 2015, 2020; Satapati et al., 2012; Wang et al., 2020) (Figures S6A and S6B).

For *ob*/*ob* mice in the fasting state, we calculated fold changes of the metabolic flux of *ob*/*ob* mice over that of WT mice for each reaction (Figure 4B, black bars). Although the TCA cycle fluxes were not precisely determined in the individual conditions including fasting WT and *ob*/*ob* mice (Figure 4A), the fold changes of the metabolic flux of fasting *ob*/*ob* mice over that of fasting WT mice were inferred with relatively narrow 95% credible intervals (0.89–1.3 average) (Figure 4B; Table S5). This would be because the metabolic fluxes inferred in WT mice were highly correlated with that in *ob*/*ob* mice. The fold changes of metabolic fluxes through reactions in gluconeogenesis (median: 2.0 on average) and the pyruvate cycle (median: 2.3 on average) were larger than those in glycogenolysis (median: 1.2 on average) and the TCA cycle (median: 1.1 on average) (Figure 4B; Table S5). The metabolic flux through G6PC, glucose production, is a sum of the metabolic flux through PGM, GPD, LDH, GPT, and glutamate dehydrogenase (GLUD) multiplied by the number of carbon atoms of the substrates. We quantified the fraction of sources of the glucose production by calculating the proportion of the metabolic flux through PGM, GPD, LDH, GPT, and GLUD to that

Please cite this article in press as: Uematsu et al., Multi-omics-based label-free metabolic flux inference reveals obesity-associated dysregulatory mechanisms in liver glucose metabolism, iScience (2022), https://doi.org/10.1016/j.isci.2022.103787

through G6PC, which represent glycogen, glycerol, lactate, alanine, and glutamate as sources, respectively (Figure 4C; Table S5). The median of the fraction of glucose production from glycerol was 34% in fasting WT mice and 45% in fasting *ob*/*ob* mice (Figure 4C; Table S5), and the 95% credible interval of the distribution of the fraction of fasting *ob*/*ob* mice minus that of fasting WT mice (5.6%–17%) was greater than zero (Figure S7A; Table S5). This result suggested that fat accumulation in the liver of *ob*/*ob* mice increased the supply of glycerol as a precursor for glucose. The median of the fraction of glucose production from alanine was 19% in fasting WT mice and 24% in fasting *ob*/*ob* mice, whereas that from lactate was 16% in WT and 13% in *ob*/*ob* mice (Figures 4C and S7A; Table S5), implying that the contributions of alanine and lactate to glucose production did not change in *ob*/*ob* mice. The median of the fraction of glucose production from glycogen was 15% in WT and 10% in *ob*/*ob* mice, whereas that from glutamate was 12% in WT mice and 5.3% in *ob*/*ob* mice. Collectively, the fraction of glucose production from glycerol increased in *ob*/*ob* mice, whereas that from glycogen and glutamate decreased. To evaluate the efficiency of using carbons of PEP for glucose production through gluconeogenesis rather than for pyruvate through the pyruvate cycle, we calculated the flux split ratios between ENO and PK reactions (Figure 4D; Table S5) and compared them between fasting WT and *ob*/*ob* mice (Figure S7B; Table S5). Compared to WT mice, the ratio of the metabolic flux through PK in *ob*/*ob* mice was higher and was similar to that through ENO, indicating less efficient use of PEP as a source of glucose in *ob*/*ob* mice than in WT mice. Because the pyruvate cycle including PK is known as a futile cycle, in which no net PEP accumulation occurs but energy is used, the increased ratio of PK flux over ENO flux in *ob*/*ob* mice is likely to cause a futile ATP dissipation through PK, PC, and PEPCK reactions. We compared the fold changes of metabolic fluxes through reactions in the glucose metabolism of *ob*/*ob* mice over that of WT mice inferred by OMELET with those in the previous metabolic flux analyses in fasting *ob*/*ob* mice (Turner et al., 2005) and high-fat diet-induced obese mice (Patterson et al., 2016; Satapati et al., 2012) (Figures S6C and S6D). With OMELET, we found a larger increase in gluconeogenic flux than that in the previous studies (Satapati et al., 2012; Turner et al., 2005), and smaller increase in glycogenolysis flux than those in the previous studies (Satapati et al., 2012; Turner et al., 2005). Other differences in glucose metabolism between WT and *ob*/*ob* mice were consistent among the four studies.

To evaluate the effect of oral glucose administration on glucose metabolism, we calculated fold changes of the metabolic fluxes after oral glucose administration over those in the fasting state in WT mice (Figure 4B, blue bars) and *ob*/*ob* mice (Figure 4B, red bars). Orally administered glucose triggered a slight increase in the metabolic fluxes through most reactions in WT mice and a decrease in *ob*/*ob* mice. An exception was the metabolic flux through PK, which did not significantly change in WT mice and decreased slightly in *ob*/*ob* mice. Neither WT nor *ob*/*ob* mice exhibited much change from the fasting state in the sources of glucose production or the flux split ratio between ENO and PK in response to oral glucose administration (Figures 4C, 4D, and S7). These results suggested the differences in the metabolic flux between WT and *ob*/*ob* mice in the fasting state were maintained after oral glucose administration. However, the effect of oral glucose on the metabolic flux was opposite within each genotype: The metabolic fluxes slightly increased in WT mice and decreased in *ob*/*ob* mice by oral glucose administration.

Contributions of regulators to changes in metabolic flux between fasting WT and *ob*/*ob* mice

Flux through reactions involved in metabolism is regulated by the enzymes, substrates, products, cofactors, and allosteric effectors. Each of these can be considered a "regulator" of the reaction. We calculated contributions of the regulators to changes in metabolic flux between the conditions (Figures 5 and S8; Table S6). The concept of the contribution is to partition the cause of changes in metabolic flux between conditions into underlying changes in the amounts of regulators. The contribution was calculated based on propagation of uncertainty of regulators' amounts to metabolic flux, and a similar approach was described in a previous study (Hackett et al., 2016) (STAR methods).

We defined contributions of regulators to changes in metabolic flux (Figure 5A). The regulators of metabolic flux were transcripts, unaccounted enzyme regulators, substrates, products, cofactors, allosteric effectors, and unaccounted flux regulators. Transcripts represent the mechanism by which changes in gene expression regulate enzyme abundance; the unaccounted 'enzyme' regulators represent other non-transcriptional mechanisms that influence the amount of enzyme such as protein degradation and stability. The unaccounted 'flux' regulators include such mechanisms as phosphorylation of enzymes and unknown allosteric effectors that were not accounted for or measured in OMELET. The contribution of regulator h to a change in metabolic flux through each reaction ψ_h was calculated as

Please cite this article in press as: Uematsu et al., Multi-omics-based label-free metabolic flux inference reveals obesity-associated dysregulatory mechanisms in liver glucose metabolism, iScience (2022), https://doi.org/10.1016/j.isci.2022.103787

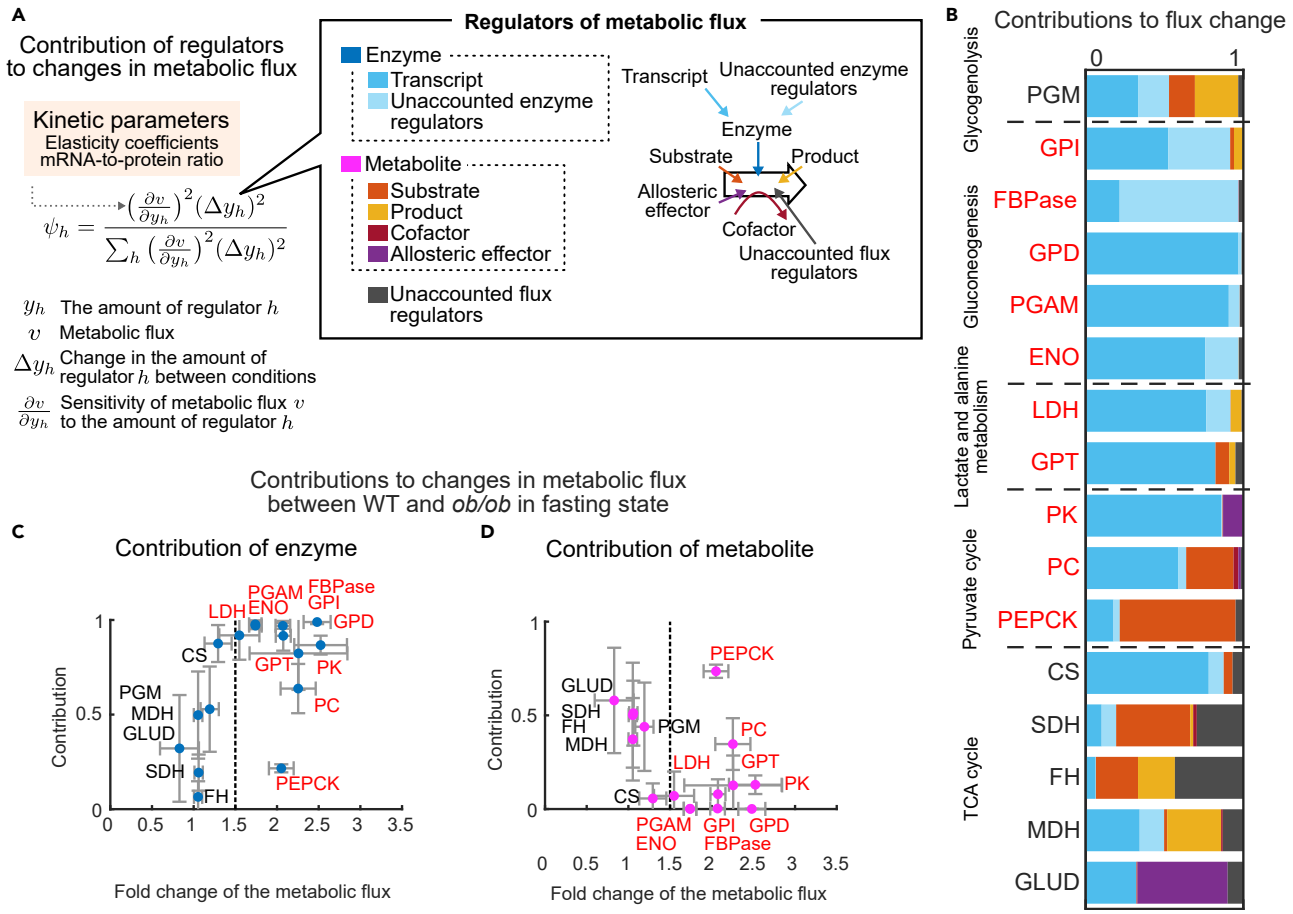

Figure 5. Contributions of regulators to changes in metabolic flux between fasting WT and *ob/ob* mice

(A) Schematic representation of contributions of regulators to changes in metabolic flux between conditions. The contribution was defined based on the sensitivity of the metabolic flux to the regulator, which is calculated using the kinetic parameters including elasticity coefficients (Figure S9; Table S5) and mRNA-to-protein ratios (Table S5), and changes in the amounts of regulators between the conditions. See also STAR methods.

(B) Contribution of regulators to changes in metabolic flux between WT and *ob/ob* mice in the fasting state. The reactions with the fold changes of the metabolic flux of *ob/ob* mice over that of WT mice in the fasting state larger than 1.5 are in red text. The stacked bars indicate the mean of the contributions independently calculated in all the Markov chain Monte Carlo samples in Figure S8. See also Table S6.

(C and D) Scatterplots illustrating the relationships between the contributions of enzyme (C) or metabolite (D) to changes in metabolic flux and the fold changes of the metabolic flux of *ob/ob* mice over that of WT mice in the fasting state. For each reaction, the mean ± SD of the distribution of the contributions of enzyme or metabolite to changes in metabolic flux (x axis) is plotted against the mean ± SD of the distribution of the fold changes of the metabolic flux of *ob/ob* mice over that of WT mice in the fasting state (y axis). The vertical gray dotted line indicates the boundary where a fold change equals 1.5. The reactions with the fold changes of the metabolic flux of *ob/ob* mice over that of WT mice in the fasting state larger than 1.5 are in red text. See also Tables S5 and S6.

$$\psi_h = \frac{\left(\frac{\partial v}{\partial y_h}\right)^2 (\Delta y_h)^2}{\sum_h \left(\frac{\partial v}{\partial y_h}\right)^2 (\Delta y_h)^2}$$

with a sensitivity of the metabolic flux to the regulator v ($\partial v/\partial y_h$) and a change in the amount of the regulator between conditions Δy_h. The contribution is calculated for changes in metabolic flux through each reaction between each pair of conditions. The sum of the contributions of all regulators to a change in metabolic flux equals one, and a larger contribution indicates a stronger regulatory effect on metabolic flux. The contribution is a normalized value for each metabolic flux, thus is independent of the magnitude of the changes in metabolic flux between the conditions. The contribution was independently calculated in all the Markov chain Monte Carlo samples and represented as a distribution (Figure S8). We focused on the regulators with a mean contribution larger than 0.25; all regulatory contributions are available in Table S6.

Please cite this article in press as: Uematsu et al., Multi-omics-based label-free metabolic flux inference reveals obesity-associated dysregulatory mechanisms in liver glucose metabolism, iScience (2022), https://doi.org/10.1016/j.isci.2022.103787

We applied this analysis to evaluate the contribution of each type of regulator, including the unaccounted flux regulators, to the difference in metabolic flux between WT and *ob*/*ob* mice in the fasting state (Figure 5B). We also examined the relationships between the contributions of enzymes or metabolites and the fold changes of the metabolic flux of *ob*/*ob* mice over that of WT mice in the fasting state (Figures 5C and 5D). For these analyses, the contribution of enzyme is the sum of its transcript and unaccounted enzyme regulators, and the contribution of metabolites is the sum of that of substrates, products, cofactors, and allosteric effectors. We found that, except for PEPCK, enzymes in the reactions with a fold change in metabolic flux greater than 1.5 in the *ob*/*ob* mice exhibited a greater contribution (Figure 5C) than did metabolites (Figure 5D). For PEPCK, the contribution of the enzyme was smaller and that of metabolites was larger. In particular, the substrate contributed the greatest effect (median: 0.73) on the increased metabolic flux through PEPCK (Figures 5B and S8; Table S6).

Quantitative *trans*-omic networks for changes in metabolic flux between WT and *ob*/*ob* mice in the fasting state

To reveal a global landscape of alteration and dysregulation of metabolic flux in fasting *ob*/*ob* mice, we constructed a quantitative *trans*-omic network by integrating the experimental data (Figure 2), the relative changes in metabolic flux (Figure 4), and the contributions of the regulators (Figure 5). The resulting network consisted of four layers (Transcript, Enzyme, Metabolic Flux, and Metabolite) (Figures 6A–6D). Nodes in the Transcript, Enzyme, Metabolic Flux, and Metabolite layer represent the transcripts, enzymes, reactions, and metabolites. Lines connecting nodes in the Transcript layer to those in the Enzyme layer represented regulation of enzymes by transcript, and those by unaccounted enzyme regulators were not displayed. Lines connecting nodes in the Enzyme layer to reactions in the Metabolic Flux layer represented the contributions of the enzyme to changes in the metabolic flux between the conditions. Lines connecting nodes in the Metabolite layer to the reactions in the Metabolic Flux layer represented regulation of changes in metabolic flux by metabolites and were color-coded according to substrate, product, cofactor, or allosteric effector. Unaccounted flux regulators were not displayed. The size of nodes represents fold changes of the corresponding molecules or reactions in *ob*/*ob* mice over those of WT mice, and the width of the lines between the layers represents the contributions of regulators to changes in metabolic flux.

We extracted the subnetworks comprised of gluconeogenesis (Figure 6C) and of the pyruvate cycle (Figure 6D), which together represented the network with median of the fold changes of the metabolic flux of *ob*/*ob* mice over that of WT mice that were larger than 1.5 (Figure 5B, red text). In the subnetwork of gluconeogenesis (Figure 6C), many transcripts, enzymes, and metabolites also increased in *ob*/*ob* mice (2.2-fold increase in metabolites, 1.9-fold in enzymes, and 1.4-fold in transcripts on average within each layer) and size of nodes were qualitatively similar among Transcript, Enzyme, and Metabolite layers. By contrast, as for edges of contribution from one layer to another, the contributions of enzymes to metabolic flux were larger than those of metabolites. On average within the subnetwork, the contribution of enzymes was 0.67, whereas the contribution of metabolites was 0.017. In addition, contributions of transcripts to enzymes were similar among many enzymes including glycerol-3-phosphate dehydrogenase 1 (Gpd1), phosphoglycerate mutase 1 (Pgam1), and enolase 1 (Eno1) except for glucose-6-phosphate isomerase 1 (Gpi1) and fructose bisphosphatase 1 (Fbp1). These results indicate a hierarchical and quantitative regulation in gluconeogenesis, where 1.4-fold increase in transcripts contributed to 79% of 2.0-fold increase in metabolic fluxes, whereas 2.2-fold increase in metabolites contributed to only 1.7% of the increase in metabolic fluxes (Figure 6E).

Pyruvate cycle consists of three reactions: PK reaction catalyzed by pyruvate kinase (Pklr) enzyme with the substrate PEP, PC reaction catalyzed by pyruvate carboxylase (Pcx) enzyme with the substrate pyruvate, and PEPCK reaction catalyzed by phosphoenolpyruvate carboxykinase 1 (Pck1) enzyme with the substrate oxaloacetate. Although fold changes in metabolic fluxes (2.5-fold for PK, 2.2-fold for PC, and 2.0-fold for PEPCK) and metabolites (1.5-fold for PEP, 1.9-fold for pyruvate, and 1.5-fold for oxaloacetate) in the subnetwork of pyruvate cycle were similar, changes in enzymes were different among reactions (Figure 6D): the enzyme Pklr increased, Pcx did not significantly change, and Pck1 decreased in *ob*/*ob* mice. These differences in fold changes of molecules resulted in different contributions to metabolic flux among PK, PC, and PEPCK. Contribution of the enzyme Pklr to the PK flux (median: 0.87) was much larger than that of the substrate PEP (median: 0.0017) and Pklr enzyme mainly caused an increase in PK flux in *ob*/*ob* mice. The medians of the contribution of Pcx enzyme and pyruvate to PC flux was 0.62 and 0.31, respectively, and both the enzyme and substrate contributed to increase in PC flux. Contribution of Pck1 enzyme to PEPCK flux

Please cite this article in press as: Uematsu et al., Multi-omics-based label-free metabolic flux inference reveals obesity-associated dysregulatory mechanisms in liver glucose metabolism, iScience (2022), https://doi.org/10.1016/j.isci.2022.103787

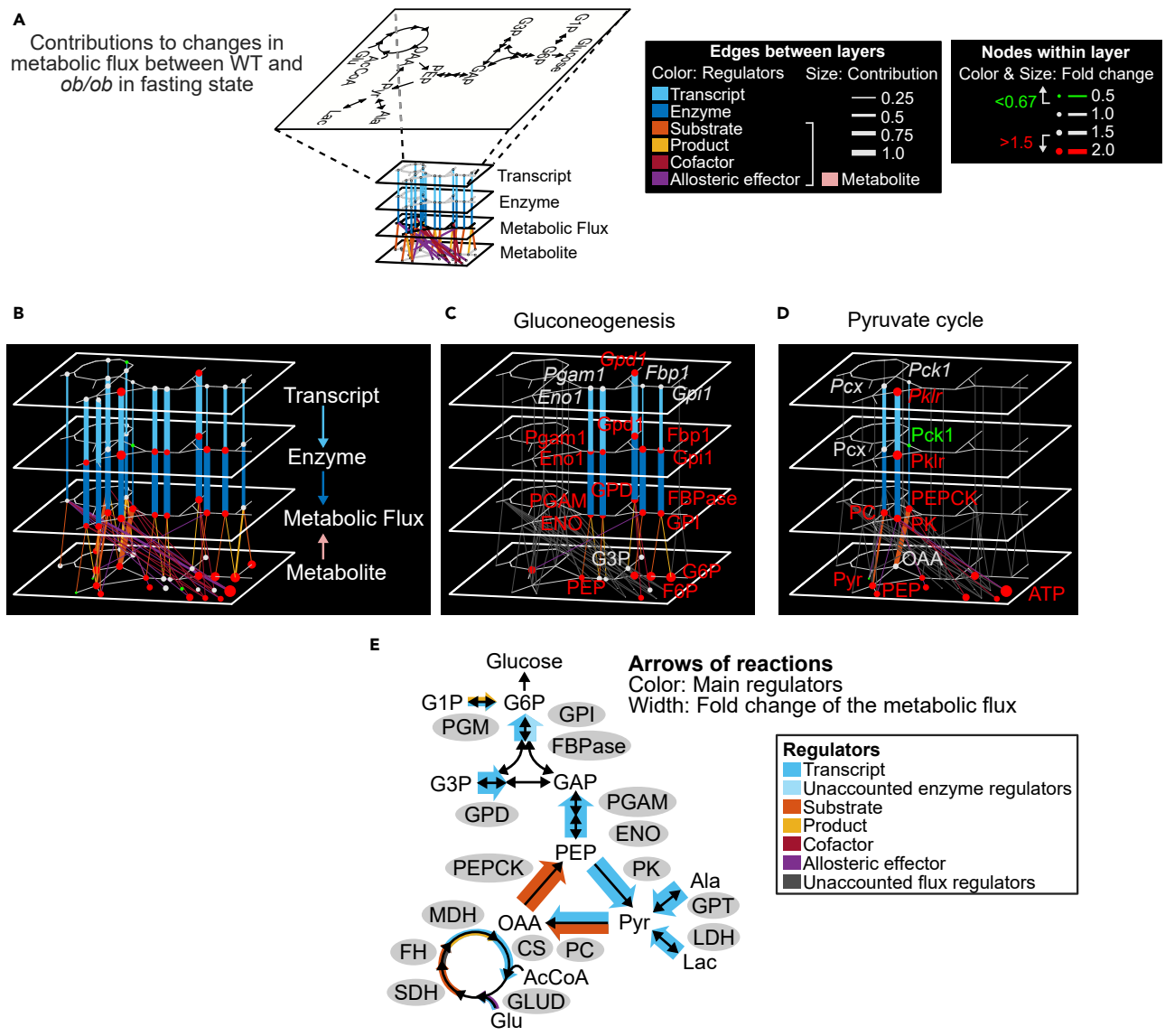

Figure 6. Quantitative trans-omic networks for changes in metabolic flux between WT and *ob/ob* mice in the fasting state

(A) Key to the quantitative *trans*-omic network for the relative difference between WT and *ob/ob* mice in the fasting state. See also Tables S2, S5, and S6.

(B) The full quantitative *trans*-omic network.

(C) The subnetwork of gluconeogenesis.

(D) The subnetwork of the pyruvate cycle.

(E) A simplified metabolic pathway with metabolic fluxes and the contributions of main regulators. The color of the arrow in each reaction indicates the main regulators, which we defined as those with a mean contribution larger than 0.25. The size of the arrow in each reaction indicates fold changes of the metabolic flux in *ob/ob* mice over those in WT mice.

(median: 0.21) was smaller than that of the substrate oxaloacetate (median: 0.74) and the substrate, rather than the enzyme, contributed to the increase in PEPCK flux. In all metabolic fluxes through PK, PC, and PEPCK in pyruvate cycle, contributions of *Pklr*, *Pcx*, and *Pck1* transcripts to Pklr, Pcx, and Pck1 enzymes (medians: 0.86, 0.59, and 0.18) were almost equal to those of Pklr, Pcx, and Pck1 enzymes to PK, PC, and PEPCK fluxes (medians: 0.87, 0.62, and 0.21), respectively, indicating that the contributions of the enzymes to changes in the metabolic flux were explained by those of the transcripts. These results suggested that the increased *Pklr* expression triggered the increased metabolic flux through the pyruvate cycle, which caused the accumulations of substrates, including pyruvate and oxaloacetate, and the large contributions of substrates to increases in metabolic fluxes through the downstream reactions of PC and PEPCK.

Please cite this article in press as: Uematsu et al., Multi-omics-based label-free metabolic flux inference reveals obesity-associated dysregulatory mechanisms in liver glucose metabolism, iScience (2022), https://doi.org/10.1016/j.isci.2022.103787

We also constructed a quantitative *trans*-omic network after oral glucose administration (Figure S10), which showed similar features with those in the fasting state. Thus, oral glucose administration had little effect on the differences in the steady state metabolic flux between WT and *ob*/*ob* mice, and on the contributions of the regulators to the differences in the metabolic flux.

Contributions of regulators to changes in metabolic flux induced by oral glucose administration within WT or *ob*/*ob* mice

We calculated the contributions of the regulators to changes in the metabolic flux by oral glucose administration in WT and *ob*/*ob* mice separately (Figures 7 and S8; Table S6). We examined the relationships between contributions of enzyme or metabolite to changes in the metabolic flux and fold changes of metabolic fluxes after oral glucose administration over those in the fasting state within each genotype (Figure 7A). None of the reactions showed a fold change of metabolic flux more than 1.5 nor less than 0.67, and no apparent relationship was found between the contributions of enzyme or metabolite and fold changes of the metabolic flux by oral glucose administration.

Among all the reactions, the largest difference in the contribution of the regulators by oral glucose administration between WT and *ob*/*ob* mice was found in PK (Figure 7B, right), a reaction with unchanged metabolic flux in WT mice and slightly decreased metabolic flux in *ob*/*ob* mice (Figure 4B). Allosteric effectors had the largest contribution to the change in metabolic flux through PK in WT mice (median: 0.55, Figures 7B and S8), whereas the *Pklr* transcript had the largest contribution in *ob*/*ob* mice (median: 0.95). These results suggested that the change in metabolic flux through PK by oral glucose administration was caused by different mechanisms between WT and *ob*/*ob* mice: changes in allosteric effectors in WT mice and changes in *Pklr* gene expression in *ob*/*ob* mice.

To explore the differences of the contributions of the regulators to the decreased metabolic flux through PK between WT and *ob*/*ob* mice, we constructed a quantitative *trans*-omic network for the relative change in metabolic flux through PK by oral glucose administration in WT mice (Figure 7C, left) and *ob*/*ob* mice (Figure 7C, middle). In WT mice, the substrate PEP and the allosteric inhibitor ATP in the Metabolite layer increased in response to oral glucose administration. The regulatory input from ATP in the Metabolite layer to PK in the Metabolic Flux layer (median: 0.50) was the largest among the regulatory inputs from the metabolites. In *ob*/*ob* mice, no metabolites in the Metabolite layer increased nor decreased following oral glucose administration. The regulatory input from Pklr in the Enzyme layer to PK in the Metabolic Flux layer (median: 0.95) was larger than regulatory inputs from metabolites, including PEP, ADP, fructose 1,6-bisphosphate (F1,6P), ATP, alanine, and phenylalanine, each of which had a regulatory input less than 0.10. The regulatory input from *Pklr* in the Transcript layer to Pklr in the Enzyme layer (median: 0.93) was almost equal to that from Pklr in the Enzyme layer to PK in the Metabolic Flux layer (median: 0.95), indicating that the contribution of enzyme was explained by that of transcript. These results suggested that the change in metabolic flux through PK was caused by increased ATP as an allosteric inhibitor in WT mice and by slightly decreased *Pklr* transcript in *ob*/*ob* mice. Given that the glucose-induced changes in metabolic flux through PK were not large (Figure 4B), we interpreted these findings to indicate that WT and *ob*/*ob* mice used different regulatory mechanisms, allosteric regulation and transcripts, respectively, to maintain the metabolic flux through PK rather than to change metabolic flux.

DISCUSSION

In this study, we developed a method OMELET to investigate alterations and dysregulation of metabolic flux in the liver that are associated with obesity. Using OMELET, we inferred the metabolic fluxes in glucose metabolism in livers of WT and *ob*/*ob* mice in the fasting state and after oral glucose administration to identify relative changes in metabolic flux between the conditions. The metabolic flux through reactions in gluconeogenesis and the pyruvate cycle increased in *ob*/*ob* mice compared to WT mice in the fasting state. The increased metabolic fluxes through reactions in gluconeogenesis were mainly caused by increased transcripts. In the pyruvate cycle, increases in transcripts mediated the increased metabolic flux through PK and increases in substrates the increase through PEPCK. In response to oral glucose administration, differences in the metabolic fluxes within mice of the same genotype were small compared to those between WT and *ob*/*ob* mice. Oral glucose administration did not change metabolic flux through PK in either WT or *ob*/*ob* mice, but the metabolic flux was regulated by increased ATP in WT mice and by decreased *Pklr* transcript in *ob*/*ob* mice. Thus, WT and *ob*/*ob* mice used different regulatory

Please cite this article in press as: Uematsu et al., Multi-omics-based label-free metabolic flux inference reveals obesity-associated dysregulatory mechanisms in liver glucose metabolism, iScience (2022), https://doi.org/10.1016/j.isci.2022.103787

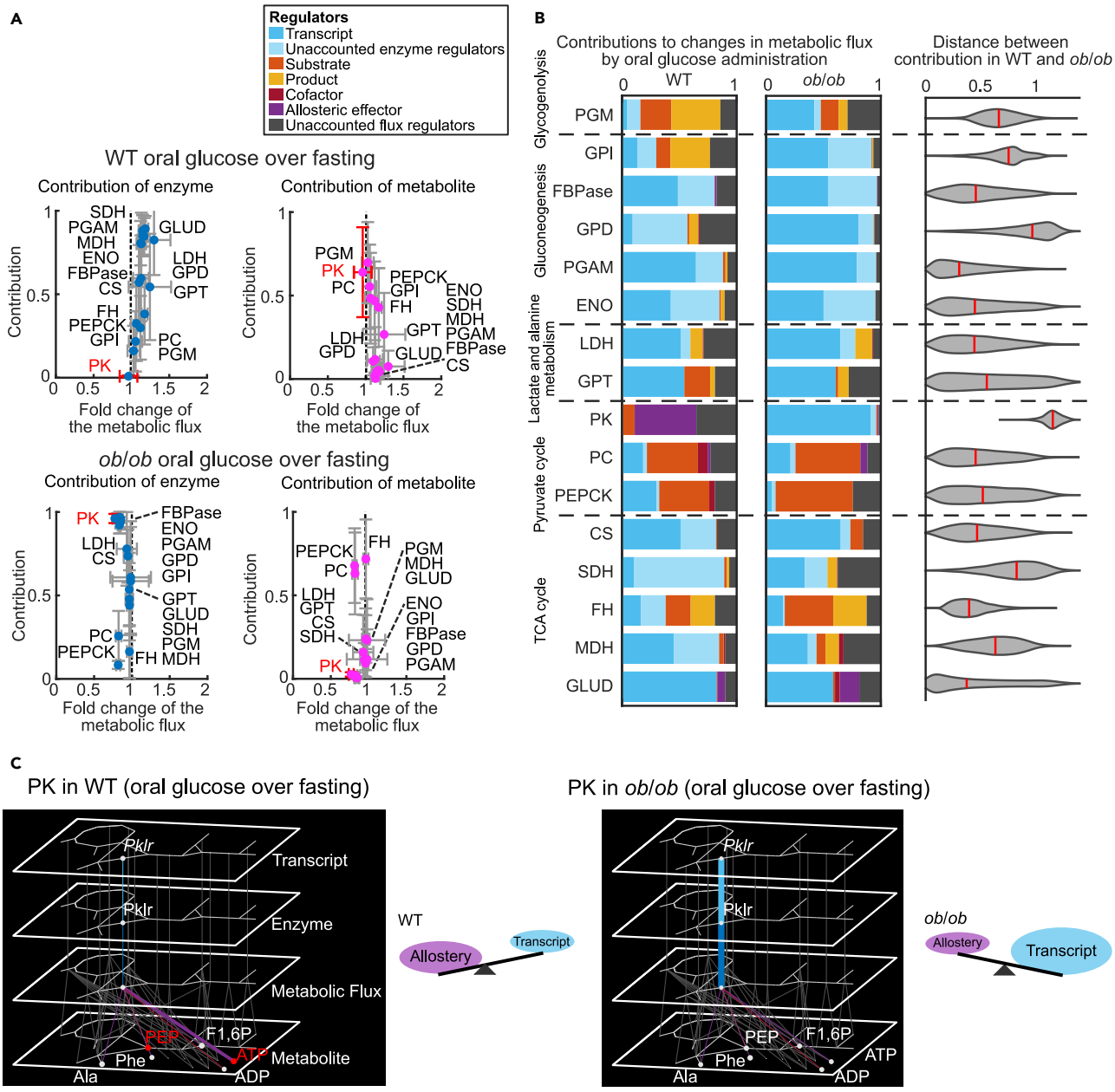

Figure 7. Contributions of regulators to changes in metabolic flux through PK by oral glucose administration

(A) Scatterplots illustrating the relationships between the contributions of enzymes and metabolites to changes in metabolic flux and the fold changes of the metabolic flux after oral glucose administration over that in the fasting state in WT mice (upper graphs) and *ob/ob* mice (lower graphs). For each reaction, the mean ± SD of the distribution of the contributions of enzyme or metabolite to changes in metabolic flux (x axis) is plotted against the mean ± SD of the distribution of the fold changes of the metabolic flux of *ob/ob* mice over that of WT mice in the fasting state (y axis). The vertical gray dotted line indicates the boundary where a fold change equals one. PK is highlighted in red.

(B) Contribution of regulators to changes in metabolic flux between fasting and after oral glucose administration in WT mice (left) and *ob/ob* mice (middle). The stacked bars indicate the mean of the contributions independently calculated in all the Markov chain Monte Carlo samples in Figure S8. The violin plot in each reaction represents the distribution of the distance quantified as L2 norm between the contribution in WT and *ob/ob* mice independently calculated in all the Markov chain Monte Carlo samples. The vertical red line in each violin plot means the median of the distribution. See also Table S6.

(C) Quantitative *trans*-omic networks for relative changes in metabolic flux through PK by oral glucose administration in WT mice and *ob/ob* mice. The networks had the same structures as those in Figure 6. Schematic representation of the main regulators to changes in metabolic flux between fasting and after oral glucose administration is displayed to the right of each network. We considered F1,6P as an allosteric activator, and ATP, alanine, and phenylalanine as allosteric inhibitors for PK in the Metabolite layer.

mechanisms, allosteric regulation and transcripts, respectively, to maintain the metabolic flux through PK rather than to change metabolic flux.

Although isotopic labeling is the current gold standard for measuring metabolic flux, it requires substantial experimental optimization of appropriate isotopic tracers, their dosages, and the time course of isotopic enrichment of metabolites. The administration method of isotopic tracers should be carefully determined depending on the biological questions (McCabe and Previs, 2004; Srivastava et al., 2016). The exchange of metabolites between multiple different organs through the blood circulation makes it difficult to precisely predict the contribution from other organs to the labeling patterns in the target organs (Fernández-García et al., 2020; Srivastava et al., 2016). Furthermore, when we investigate metabolism in fasted mice which external nutrients do not come into, the addition of isotopic tracers can perturb the relevant metabolic flux, resulting in different metabolic states (Previs and Kelley, 2015). For example, when ^{13}C-propionate or ^{13}C-lactate is used as an isotopic tracer for measurement of gluconeogenic flux in fasted mice, the measured metabolic fluxes differ between tracers because the administration of ^{13}C-propionate increases metabolic flux through the pyruvate cycle (Perry et al., 2016). In contrast, the use of multi-omic data to infer metabolic fluxes reduces the complexity in the current standard isotopic labeling experiments regarding the experimental optimization, administration of isotopic tracers, and metabolite exchanges between different organs. Furthermore, the metabolomic, proteomic, and transcriptomic data provide not only the metabolic flux through individual reactions but also the regulation of metabolic flux from multiple molecules. Therefore, although isotopic labeling is certainly the current best way to study metabolic fluxes, OMELET can be an alternative tool to investigate metabolic flux without using isotopic labeling. However, the accuracy of inference of metabolic flux without isotopic labeling data needs to be validated. We validated the performance of OMELET by applying it to the simulated datasets from kinetic models of the hepatocyte glucose metabolism (Marín-Hernández et al., 2020) and yeast glycolysis (Messiha et al., 2014; Smallbone et al., 2013) (Figure S2). We also applied OMELET to the data in fasting mouse liver and found that the inferred metabolic fluxes in WT mice were consistent with those in the previous studies (Figures S6A and S6B). The fold changes of the metabolic fluxes through most reactions in the glucose metabolism of *ob*/*ob* mice over that of WT mice inferred by OMELET were consistent with those in the previous studies, except for that through glycogenolysis (Figures S6C and S6D). These results suggested that the experimental data of the amounts of enzymes and metabolites would contain some, if not sufficient, information on metabolic fluxes as latent parameters, which can be inferred by OMELET. One disadvantage of using multi-omic data to infer metabolic fluxes based on kinetic modeling is that many assumptions including reaction kinetics and regulations underlie in kinetic modeling. In addition, kinetic modeling requires more number of parameters such as turnover rate, dissociation constant of metabolites, equilibrium constants, and elasticity coefficients compared to a general metabolic flux analysis using isotopic tracers, which makes the optimization of parameters difficult in kinetic modeling using multi-omic data.

OMELET is a kind of kinetic modeling framework of metabolism. Although mechanistic kinetic models of metabolism enable a quantitative understanding of metabolic flux and its regulation, the difficulty in obtaining kinetic parameters especially in intact cells or tissues has been a major drawback. To overcome this challenge, advanced kinetic modeling frameworks have been developed (Saa and Nielsen, 2017), including Optimization and Risk Analysis of Complex Living Entities (ORACLE) (Miskovic and Hatzimanikatis, 2010), General Reaction and Assembly Platform (GRASP) (Saa and Nielsen, 2015), Ensemble Modeling (EM) (Tran et al., 2008), and Mass Action Stoichiometric Simulation (MASS) (Jamshidi and Palsson, 2008). In comparison with these kinetic modeling frameworks, OMELET is characterized by several features including both advantages and disadvantages. The major advantage of OMELET is that it can infer metabolic fluxes from metabolomic and proteomic data (and transcriptomic data if available), whereas most kinetic modeling frameworks infer kinetic parameters using metabolic fluxes as inputs which are experimentally measured or inferred by constraint-based modeling. OMELET infers relative changes in metabolic flux between conditions using relative quantification of metabolites, enzymes (and transcripts if available) instead of absolute quantification, which is more difficult to obtain than relative quantification. Another important feature is that OMELET can quantitatively integrate several omic layers based on kinetic equations. Such multi-omic integration into one mathematical framework is still very challenging even in the advanced kinetic modeling frameworks described above. Furthermore, OMELET does not require the description of reaction kinetics for all the reactions in the metabolic pathway of interest: only a subset of reactions associated with measured metabolites and enzymes needs to be described in reaction kinetics. The existing kinetic modeling frameworks require the description of reaction kinetics in all the reactions.

However, the occurrence of missing data in multi-omic studies increases uncertainty of parameters and simulation results in mathematical modeling. In contrast, OMELET attempts to overcome this problem by omitting descriptions of reactions kinetics for reactions whose regulator amounts are not measured, which reduces the uncertainty of inferred metabolic fluxes and contributions of regulators. One of the disadvantages of OMELET is that OMELET cannot be used to predict the metabolic state under specific perturbations to kinetic parameters because of the lack of kinetic descriptions for a part of the metabolic reactions in the pathway. Another disadvantage is that OMELET does not explicitly consider thermodynamic constraints on metabolic fluxes and kinetic parameters as ORACLE and GRASP do. The thermodynamic constraints could be incorporated into OMELET as priors for them in the future.

We used the simultaneously obtained experimental dataset of the amounts of metabolites, enzymes, and transcripts from the same samples for OMELET. Using simultaneously obtained multi-omic data, a Bayesian method has the potential to analyze metabolic flux (Heinonen et al., 2019) and its regulation (Hackett et al., 2016; John et al., 2019; Saa and Nielsen, 2016). Such datasets enabled us to apply a Bayesian method rather than analyzing the population mean. A Bayesian method can incorporate uncertainties inherent in the experimental data, such as measurement noise and population heterogeneity. Based on a Bayesian method, we assumed the experimental data resulted from a generative model that described the underlying processes given latent parameters, and evaluated the probability that the model yields the data by likelihood. In OMELET, the enzymes were derived from a generative model based on metabolic flux, and the transcripts from a generative model based on protein turnover (Figure 3). Using these two generative models in OMELET, we evaluated the likelihood of the enzymes and transcripts from each mouse to infer unknown parameters including metabolic fluxes, elasticity coefficients and mRNA-to-protein ratios.

OMELET does not require kinetic and thermodynamic parameters that have already been reported for the metabolic pathway of interest. There are two reasons why we inferred kinetic parameters in OMELET. The first reason is that most kinetic parameters have been determined in isolated enzymes and it is unclear whether they reflect enzyme behavior in intake cells or tissues under the experimental conditions we analyze (Davidia et al., 2016; Heckmann et al., 2020; Teusink et al., 2000). The parameter values depend on many factors such as tissue types or experimental and physiological conditions. The second reason is that, thanks to the minimal information requirement, OMELET is not specific to the glucose metabolism whose kinetic parameters are well characterized but applicable to different metabolic networks in different species whose kinetic parameters are not well characterized.

Using OMELET, we found altered and dysregulated metabolic flux associated with obesity. We found that the large increase in metabolic flux through reactions in gluconeogenesis in *ob*/*ob* mice compared to WT mice in the fasting state was mainly caused by increased gene expression of the enzymes (Figure 6). There are several transcription factors (TFs) involved in controlling the expression of genes encoding enzymes involved in gluconeogenesis. For example, cAMP response element-binding protein (CREB) activates transcription of *G6pc* and *Fbp1* (Hanson and Reshef, 1997; Herzig et al., 2001), as well as *Gpi1* and *Pgam1* (Everett et al., 2013). Liver-specific knockdown of CREB reduced fasting plasma glucose concentrations in *ob*/*ob* mice through downregulation of *G6pc* and *Fbp1* (Erion et al., 2009). In addition to these key TFs identified by individual experiments, high-throughput measurements and multi-omic analyses have revealed many more TFs involved in metabolic alteration associated with obesity (Egami et al., 2021; Kokaji et al., 2020; Soltis et al., 2017). Although TFs contribute to changes in metabolic flux in glucose metabolism associated with obesity, metabolic flux is also regulated by metabolites that include substrates, products, cofactors, and allosteric effectors. In this study, we found that transcripts, rather than metabolites, mainly contributed to the differences in the metabolic flux through reactions in gluconeogenesis except for GPI and FBPase between WT and *ob*/*ob* mice (Figure 4). Our results suggested that TFs would trigger increased gluconeogenic flux associated with obesity by promoting the expression of the genes encoding the relevant metabolic enzymes.

In the pyruvate cycle, increased oxaloacetate (a substrate), rather than Pck1, contributed to the increased metabolic flux through PEPCK in fasting *ob*/*ob* mice (Figure 6D). Several metabolic flux analyses showed that the metabolic flux through PEPCK increased associated with obesity (Patterson et al., 2016; Satapati et al., 2012; Sunny et al., 2011), which was consistent with our data. Given that PEPCK is an irreversible reaction and there are no known allosteric effectors, possible regulators of the metabolic flux through PEPCK include Pck1 amounts, the substrate oxaloacetate, and the cofactor GTP. However, it has been unclear which regulator mainly contributed the increased metabolic flux through PEPCK associated with obesity.

Please cite this article in press as: Uematsu et al., Multi-omics-based label-free metabolic flux inference reveals obesity-associated dysregulatory mechanisms in liver glucose metabolism, iScience (2022), https://doi.org/10.1016/j.isci.2022.103787

Among the possible regulators, Pck1 amounts decreased associated with obesity in the fasting state (Samuel et al., 2009; Satapati et al., 2012; Sunny et al., 2011), which was observed in our proteomic data (Figure 2). These studies suggest that the increased metabolic flux is not consistent with the decreased Pck1 amount. Here, we found that increased oxaloacetate, although inferred as parameters, was responsible for the increased metabolic flux through PEPCK (Figure 6D), which provides a mechanistic explanation for the increased metabolic flux through PEPCK that is associated with obesity.

The only difference in the contributions of regulators to the changes following oral glucose administration between WT and *ob*/*ob* mice was in metabolic flux through PK (Figure 7). In WT mice, the allosteric effector ATP was the largest contributor to the slightly decreased PK flux. In *ob*/*ob* mice, a reduction in *Pklr* transcript was the largest regulatory contributor. A reason why allosteric regulation was not the main regulator in *ob*/*ob* mice may be because amounts of allosteric effectors, such as ATP, were high even in the fasting state and did not increase following oral glucose administration (Figure 2).

In calculating the contributions of regulators to changes in metabolic flux between the conditions, we considered unaccounted flux regulators as one of the regulators of metabolic flux and unaccounted enzyme regulators as one of the regulators of enzymes. The contributions of unaccounted flux regulators to changes in metabolic flux between fasting WT and *ob*/*ob* mice were smaller than those of other regulators in all the reactions in gluconeogenesis and the pyruvate cycle, indicating that changes in metabolic fluxes through these reactions can be explained by known regulators that we considered (Figures 5B and S8). In contrast, the contributions of unaccounted enzyme regulators to changes in enzyme in reactions through GPI and FBPase were relatively larger than those through other reactions, indicating that the increase in enzyme in *ob*/*ob* mice cannot be explained by the transcripts. Although we used a simple linear relationship between the amount of an enzyme and a transcript in OMELET, an increase in enzyme that is not accompanied by the changes in transcripts should be explained by other regulatory mechanisms, such as changes in protein stability. Furthermore, the contributions of unaccounted flux regulators to changes in metabolic flux between fasting and after oral glucose administration were larger in many reactions than those between fasting WT and *ob*/*ob* mice (Figures 7B and S8). To explain the contributions of unaccounted flux regulators, we need to consider posttranslational modifications, such as phosphorylation, of enzymes. Such data can be incorporated by including phosphoproteomic data.

It is important to consider that binding of metabolites to TFs can regulate gene expression. In this study, however, we did not model the influence of metabolites on transcript levels via TF regulation. To incorporate the regulation of gene expression by binding of metabolites to TFs into OMELET, metabolite-TF, and TF-gene interactions with information on activation or inhibition should be specified. The expression of transcript amounts as a function of metabolites in a steady state would enable us to evaluate the likelihood of the transcript amounts (Bhattacharya et al., 2014). A major difficulty would be insufficient biological knowledge about metabolite-TF and TF-gene interactions. Another difficulty would lie in parameter estimation for modeling the complex regulation of gene expression just from metabolomic and transcriptomic data. Additional experimental data such as protein amounts of TFs, promoter activities of target genes, and chromatin states would be needed (Yugi et al., 2019). Although metabolite-TF and TF-gene interactions can regulate gene expression, the inclusion of TFs regulated by metabolites would have little effect on our metabolic flux inference and calculation of contributions to changes in metabolic flux between conditions because the amounts of transcripts were directly given by the experimental data.

In conclusion, we developed OMELET, which uses the simultaneously obtained multi-omic data to infer metabolic fluxes in the glucose metabolism in multiple conditions and to identify changes in metabolic flux between the conditions. Furthermore, we calculated the contributions of the regulators to the changes in metabolic flux between the conditions. OMELET is designed to infer metabolic flux without using isotopic labeling data and to simultaneously infer changes in metabolic flux and the contributions of regulators. The quantitative *trans*-omic network provided insights into the obesity-associated changes in the glucose metabolism in liver and revealed comprehensive molecular mechanisms for understanding the pathology of alteration and dysregulation of metabolic flux associated with obesity.

Limitations of the study

There are several limitations of this study. We did not examine enzyme activities (Vmax or kcat) and assumed that kcat is constant: the change in metabolic flux is proportional to the change in enzyme amount

when the amounts of metabolites are constant. Although we considered unaccounted flux regulators, which reflect enzyme activities not explained by enzyme amounts, the measurement of actual enzyme activities would be important to understand the regulation of metabolic flux by enzymes. In addition, variation of one enzyme is not always correlated with the variation of its coding transcript across different conditions, but we assumed a nearly linear relationship between enzyme and transcript changes to simplify the modeling (Liu et al., 2016; Lundberg, 2010)). Changes in enzyme amounts that cannot be explained by changes in transcript amounts under the linear assumption, such as Gpi1 and Fbp1, can be explained by unaccounted enzyme regulators in OMELET. Nevertheless, incorporating other processes that contribute to changes in enzyme amounts including protein stability and translation rate would facilitate more accurate modeling of OMELET. The 95% credible intervals of the metabolic fluxes in the TCA cycle were large compared to those through other reactions in glucose metabolism (Figures 4A and S4), indicating that the metabolic fluxes in the TCA cycle were not precisely determined. The large credible intervals of the inferred metabolic fluxes in the TCA cycle may be because of small changes in the amounts of enzymes and metabolites in the TCA cycle between the conditions. Alternatively, the large credible intervals of the inferred metabolic fluxes in the TCA cycle may be because we did not consider the compartmentation of reactions into cytosol and mitochondria, and inferred metabolic fluxes averaged in a whole cell. Concentrations of several metabolites, especially citrate and α-ketoglutarate, could differ between cytosol and mitochondria (Chen et al., 2016; Lee et al., 2019), which may affect the calculation of metabolic fluxes and contributions to the changes in metabolic fluxes between conditions. In addition, OMELET is based on a steady state assumption and cannot infer dynamic changes in metabolic flux under nonsteady state conditions.

STAR★METHODS

Detailed methods are provided in the online version of this paper and include the following:

- KEY RESOURCES TABLE
- RESOURCE AVAILABILITY
  - Lead contact
  - Materials availability
  - Data and code availability
- EXPERIMENTAL MODEL AND SUBJECT DETAILS
  - Animals
- METHOD DETAILS
  - Metabolic network for glucose metabolism in mice
  - Algorithm of OMELET
  - Application of OMELET to mouse data
  - Parameter estimation
  - Simulation using hepatocyte kinetic model
  - Simulation using yeast kinetic model
  - Contributions of regulators to flux changes
  - Metabolomic analysis
  - Proteomic analysis
  - Transcriptomic analysis
  - Blood glucose and insulin
- QUANTIFICATION AND STATISTICAL ANALYSIS

SUPPLEMENTAL INFORMATION

Supplemental information can be found online at https://doi.org/10.1016/j.isci.2022.103787.

ACKNOWLEDGMENTS

We are grateful to Maki Ohishi, Ayano Ueno, Keiko Endo, Sanae Ashitani, Keiko Kato, and Kaori Saitoh (Keio University) for their technical assistance with metabolomic analysis using CE-MS. We thank Shinsuke Uda of Kyushu University and our laboratory members for critically reading this manuscript and for their technical assistance with the experiments. The computational analysis of this work was performed in part with support of the supercomputer system of National Institute of Genetics (NIG), Research Organization of Information and Systems (ROIS). This manuscript was edited by Nancy R. Gough (BioSerendipity, LLC).

This work was supported by the Japan Society for the Promotion of Science KAKENHI (JP17H06300, JP17H06299, JP18H03979, JP21H04759), the Japan Science and Technology Agency (JST) (JPMJCR2123), and by The Uehara Memorial Foundation. S.U. receives funding from JSPS KAKENHI Grant Number JP19J22134. S.O. receives funding from a Grant-in-Aid for Early-Career Scientists (JP17K14864 and JP21K14467). A. Hatano is supported by Grant-in-Aid from the Tokyo Biochemical Research Foundation. T.K. receives funding from JSPS KAKENHI Grant Number JP21K16349. H.K. was supported by JSPS KAKENHI JP20H03237. Y.S. was supported by the JSPS KAKENHI Grant Number JP17H06306. K.I.N. was supported by the JSPS KAKENHI Grant Number JP17H06301, JP18H05215. A. Hirayama was supported by the JSPS KAKENHI Grant Number JP18H04804. T.S. receives funding from the AMED from the Japan Agency for Medical Research and Development under Grant Number JP18gm0710003.

AUTHOR CONTRIBUTIONS

S.U., S.O., and S.K. conceived the project; A. Hatano, T.K., Y.I., H.K., M.M., and K.I.N. designed and performed the animal experiments; A. Hirayama and T.S. performed metabolomic analysis using CE-MS; Y.S. performed transcriptomic analysis using RNA-seq; M.M. and K.I.N. performed proteomic analysis using LC-MS/MS; S.U., S.O., K.T., A. Hatano, T.K., Y.I., and K.H. analyzed the data; S.U., S.O., and K.T. performed mathematical modeling analyses. S.U., S.O., and S.K. wrote the manuscript. All authors read and approved the final manuscript.

DECLARATION OF INTERESTS

The authors declare no competing interests.

Received: September 6, 2021
Revised: December 1, 2021
Accepted: January 13, 2022
Published: February 18, 2022

REFERENCES

Antoniewicz, M.R. (2018). A guide to 13C metabolic flux analysis for the cancer biologist. Exp. Mol. Med. *50*, 1–13.

Beylot, M., Soloviev, M.V., David, F., Landau, B.R., and Brunengraber, H. (1995). Tracing hepatic gluconeogenesis relative to citric acid cycle activity in vitro and in vivo: comparisons in the use of [3-13C]lactate, [2-13C]acetate, and α-keto[3-13C]isocaproate. J. Biol. Chem. *270*, 1509–1514.

Bhattacharya, B.S., Sweby, P.K., Minihane, A.M., Jackson, K.G., and Tindall, M.J. (2014). A mathematical model of the sterol regulatory element binding protein 2 cholesterol biosynthesis pathway. J. Theor. Biol. *349*, 150–162.

Burgess, S.C., Jeffrey, F.M.H., Storey, C., Milde, A., Hausler, N., Merritt, M.E., Mulder, H., Holm, C., Sherry, A.D., and Malloy, C.R. (2005). Effect of murine strain on metabolic pathways of glucose production after brief or prolonged fasting. Am. J. Physiol. Metab. *289*, E53–E61.

Burgess, S.C., Merritt, M.E., Jones, J.G., Browning, J.D., Sherry, A.D., and Malloy, C.R. (2015). Limitations of detection of anaplerosis and pyruvate cycling from metabolism of [1-13 C] acetate. Nat. Med. *21*, 108–109.

Charlton, M. (2004). Nonalcoholic fatty liver disease: a review of current understanding and future impact. Clin. Gastroenterol. Hepatol. *2*, 1048–1058.

Chen, W.W., Freinkman, E., Wang, T., Birsoy, K., and Sabatini, D.M. (2016). Absolute quantification of matrix metabolites reveals the dynamics of mitochondrial metabolism. Cell *166*, 1324–1337.e11.

Childs, D., Grimbs, S., and Selbig, J. (2015). Refined elasticity sampling for Monte Carlo-based identification of stabilizing network patterns. Bioinformatics *31*, i214–i220.

Cunningham, F., Amode, M.R., Barrell, D., Beal, K., Billis, K., Brent, S., Carvalho-Silva, D., Clapham, P., Coates, G., Fitzgerald, S., et al. (2015). Ensembl 2015. Nucleic Acids Res. *43*, D662–D669.

Davidia, D., Noorb, E., Liebermeisterc, W., Bar-Evend, A., Flamholze, A., Tummlerf, K., Barenholza, U., Goldenfelda, M., Shlomig, T., and Miloa, R. (2016). Global characterization of in vivo enzyme catalytic rates and their correspondence to in vitro kcat measurements. Proc. Natl. Acad. Sci. U S A *113*, 3401–3406.

Egami, R., Kokaji, T., Hatano, A., Yugi, K., Eto, M., Morita, K., Ohno, S., Fujii, M., Hironaka, K., Uematsu, S., et al. (2021). Trans-omic analysis reveals obesity-associated dysregulation of inter-organ metabolic cycles between the liver and skeletal muscle. IScience *24*, 102217.

Erion, D.M., Ignatova, I.D., Yonemitsu, S., Nagai, Y., Chatterjee, P., Weismann, D., Hsiao, J.J., Zhang, D., Iwasaki, T., Stark, R., et al. (2009). Prevention of hepatic steatosis and hepatic insulin resistance by knockdown of cAMP response element-binding protein. Cell Metab. *10*, 499–506.

Everett, L.J., Lay, J.L., Lukovac, S., Bernstein, D., Steger, D.J., Lazar, M.A., and Kaestner, K.H. (2013). Integrative genomic analysis of CREB defines a critical role for transcription factor networks in mediating the fed/fasted switch in liver. BMC Genomics *14*, 337.

Fernández-García, J., Altea-Manzano, P., Pranzini, E., and Fendt, S.M. (2020). Stable isotopes for tracing mammalian-cell metabolism in vivo. Trends Biochem. Sci. *45*, 185–201.

Flicek, P., Amode, M.R., Barrell, D., Beal, K., Billis, K., Brent, S., Carvalho-Silva, D., Clapham, P., Coates, G., Fitzgerald, S., et al. (2014). Ensembl 2014. Nucleic Acids Res. *42*, D749–D755.

Hackett, S.R., Zanotelli, V.R.T., Xu, W., Goya, J., Park, J.O., Perlman, D.H., Gibney, P.A., Botstein, D., Storey, J.D., and Rabinowitz, J.D. (2016). Systems-level analysis of mechanisms regulating yeast metabolic flux. Science *354*, aaf2786.

Han, H.S., Kang, G., Kim, J.S., Choi, B.H., and Koo, S.H. (2016). Regulation of glucose metabolism from a liver-centric perspective. Exp. Mol. Med. *48*, 1–10.

Hanson, R.W., and Reshef, L. (1997). Regulation of Phosphoenolpyruvate carbozykinase (GTP) gene expression. Annu. Rev. Biochem. *66*, 581–611.

Hasenour, C.M., Wall, M.L., Ridley, D.E., Hughey, C.C., James, F.D., Wasserman, D.H., and Young, J.D. (2015). Mass spectrometry-based microassay of 2H and 13C plasma glucose labelling to quantify liver metabolic fluxes in vivo. Am. J. Physiol. Endocrinol. Metab. *309*, E191–E203.

Hasenour, C.M., Rahim, M., and Young, J.D. (2020). In vivo estimates of liver metabolic flux assessed by 13C-propionate and 13C-lactate are impacted by tracer recycling and equilibrium assumptions. Cell Rep. *32*, 107986.

Heckmann, D., Campeau, A., Lloyd, C.J., Phaneuf, P.V., Hefner, Y., Carrillo-Terrazas, M., Feist, A.M., Gonzalez, D.J., and Palsson, B.O. (2020). Kinetic profiling of metabolic specialists demonstrates stability and consistency of in vivo enzyme turnover numbers. Proc. Natl. Acad. Sci. U S A *117*, 23182–23190.

Heinonen, M., Osmala, M., Mannerström, H., Wallenius, J., Kaski, S., Rousu, J., and Lähdesmäki, H. (2019). Bayesian metabolic flux analysis reveals intracellular flux couplings. Bioinformatics *35*, i548–i557.

Herzig, S., Long, F., Jhala, U.S., Hedrick, S., Quinn, R., Bauer, A., Rudolph, D., Schutz, G., Yoon, C., Puigserver, P., et al. (2001). CREB regulates hepatic gluconeogenesis through the coactivator PGC-1. Nature *413*, 179–183.

Hiller, K., and Metallo, C.M. (2013). Profiling metabolic networks to study cancer metabolism. Curr. Opin. Biotechnol. *24*, 60–68.

Hoffman, M.D., and Gelman, A. (2014). The no-U-turn sampler: adaptively setting path lengths in Hamiltonian Monte Carlo. J. Mach. Learn. Res. *15*, 1593–1623.

Hoops, S., Gauges, R., Lee, C., Pahle, J., Simus, N., Singhal, M., Xu, L., Mendes, P., and Kummer, U. (2006). COPASI - a complex pathway simulator. Bioinformatics *22*, 3067–3074.

Hotamisligil, G.S., and Erbay, E. (2008). Nutrient sensing and inflammation in metabolic diseases. Nat. Rev. Immunol. *8*, 923–934.

Hucka, M., Finney, A., Sauro, H.M., Bolouri, H., Doyle, J.C., Kitano, H., Arkin, A.P., Bornstein, B.J., Bray, D., Cornish-Bowden, A., et al. (2003). The systems biology markup language (SBML): a medium for representation and exchange of biochemical network models. Bioinformatics *19*, 524–531.

Jamshidi, N., and Palsson, B. (2008). Formulating genome-scale kinetic models in the post-genome era. Mol. Syst. Biol. *4*, 171.

Jang, C., Chen, L., and Rabinowitz, J.D. (2018). Metabolomics and isotope tracing. Cell *173*, 822–837.

Jin, E.S., Uyeda, K., Kawaguchi, T., Burgess, S.C., Malloy, C.R., and Sherry, D.D. (2003). Increased hepatic fructose 2,6-bisphosphate after an oral glucose load does not affect gluconeogenesis. J. Biol. Chem. *278*, 28427–28433.

Jin, E.S., Beddow, S.A., Malloy, C.R., and Samuel, V.T. (2013). Hepatic glucose production pathways after three days of a high-fat diet. Metabolism *62*, 152–162.

John, P.C.S., Strutz, J., Broadbelt, L.J., Tyo, K.E.J., and Bomble, Y.J. (2019). Bayesian inference of metabolic kinetics from genome-scale multiomics data. PLoS Comput. Biol. *15*, 1–23.

Jones, J.G., Naidoo, R., Sherry, A.D., Jeffrey, F.M.H., Cottam, G.L., and Malloy, C.R. (1997). Measurement of gluconeogenesis and pyruvate recycling in the rat liver: a simple analysis of glucose and glutamate isotopomers during metabolism of [1,2,3-13C3]propionate. FEBS Lett. *412*, 131–137.

Kacser, H., and Burns, J.A. (1995). The control of flux. Biochem. Soc. Trans. *23*, 341–366.

Kahn, S.E., Hull, R.L., and Utzschneider, K.M. (2006). Mechanisms linking obesity to insulin resistance and type 2 diabetes. Nature *444*, 840–846.

Katz, J., Wals, P., and Lee, W.N.P. (1993). Isotopomer studies of gluconeogenesis and the Krebs cycle with 13C- labeled lactate. J. Biol. Chem. *268*, 25509–25521.

Kawata, K., Hatano, A., Yugi, K., Kubota, H., Sano, T., Fujii, M., Tomizawa, Y., Kokaji, T., Tanaka, K.Y., Uda, S., et al. (2018). Trans-omic analysis reveals selective responses to induced and basal insulin across signaling, transcriptional, and metabolic networks. IScience *7*, 212–229.

Kokaji, T., Hatano, A., Ito, Y., Yugi, K., Eto, M., Morita, K., Ohno, S., Fujii, M., Hironaka, K.I., Egami, R., et al. (2020). Transomics analysis reveals allosteric and gene regulation axes for altered hepatic glucose-responsive metabolism in obesity. Sci. Signal. *13*, eaaz1236.

Large, V., Brunengraber, H., Odeon, M., and Beylot, M. (1997). Use of labeling pattern of liver glutamate to calculate rates of citric acid cycle and gluconeogenesis. Am. J. Physiol. *272*, E51–E58.

Lee, W.D., Mukha, D., Aizenshtein, E., and Shlomi, T. (2019). Spatial-fluxomics provides a subcellular-compartmentalized view of reductive glutamine metabolism in cancer cells. Nat. Commun. *10*, 1351.

Liu, Y., Beyer, A., and Aebersold, R. (2016). On the Dependency of Cellular Protein Levels on mRNA Abundance, *165* (Cell. Elsevier Inc), pp. 535–550. https://doi.org/10.1016/j.cell.2016.03.014.

Lundberg, E., et al. (2010). Defining the transcriptome and proteome in three functionally different human cell lines. Molecular Systems Biology *6* (450), 1–9. https://doi.org/10.1038/msb.2010.106.

Marín-Hernández, Á., Gallardo-Pérez, J.C., Reyes-García, M.A., Sosa-Garrocho, M., Macías-Silva, M., Rodríguez-Enríquez, S., Moreno-Sánchez, R., and Saavedra, E. (2020). Kinetic modeling of glucose central metabolism in hepatocytes and hepatoma cells. Biochim. Biophys. Acta Gen. Subj. *1864*, 129687.

Matsumoto, M., Pocai, A., Rossetti, L., DePinho, R.A., and Accili, D. (2007). Impaired regulation of hepatic glucose production in mice lacking the forkhead transcription factor Foxo1 in liver. Cell Metab. *6*, 208–216.

Matsumoto, M., Matsuzaki, F., Oshikawa, K., Goshima, N., Mori, M., Kawamura, Y., Ogawa, K., Fukuda, E., Nakatsumi, H., Natsume, T., et al. (2017). A large-scale targeted proteomics assay resource based on an in vitro human proteome. Nat. Methods *14*, 251–258.

McCabe, B.J., and Previs, S.F. (2004). Using isotope tracers to study metabolism: application in mouse models. Metab. Eng. *6*, 25–35.

Merkel, D. (2014). Docker: lightweight linux containers for consistent development and deployment. Linux J. *2014*, 2.

Messiha, H.L., Kent, E., Malys, N., Carroll, K.M., Swainston, N., Mendes, P., and Smallbone, K. (2014). Enzyme characterisation and kinetic modelling of the pentose 1 phosphate pathway in yeast 2 network-scale models by merging smaller pathway-scale models. PeerJ. Prepr. *2*, e146v4.

Miskovic, L., and Hatzimanikatis, V. (2010). Production of biofuels and biochemicals: in need of an ORACLE. Trends Biotechnol. *28*, 391–397.

Nordlie, R.C., Foster, J.D., and Lange, A.J. (1999). Regulation of glucose production by the liver. Annu. Rev. Nutr. *19*, 379–406.

Le Novère, N., Bornstein, B., Broicher, A., Courtot, M., Donizelli, M., Dharuri, H., Li, L., Sauro, H., Schilstra, M., Shapiro, B., et al. (2006). BioModels Database: a free, centralized database of curated, published, quantitative kinetic models of biochemical and cellular systems. Nucleic Acids Res. *34*, D689–D691.

Ohno, S., Quek, L.E., Krycer, J.R., Yugi, K., Hirayama, A., Ikeda, S., Shoji, F., Suzuki, K., Soga, T., James, D.E., et al. (2020). Kinetic trans-omic analysis reveals key regulatory mechanisms for insulin-regulated glucose metabolism in adipocytes. iScience *23*, 101479.

Patterson, R.E., Kalavalapalli, S., Williams, C.M., Nautiyal, M., Mathew, J.T., Martinez, J., Reinhard, M.K., McDougall, D.J., Rocca, J.R., Yost, R.A., et al. (2016). Lipotoxicity in steatohepatitis occurs despite an increase in tricarboxylic acid cycle activity. Am. J. Physiol. Endocrinol. Metab. *310*, E484–E494.

Perry, R.J., Borders, C.B., Cline, G.W., Zhang, X.M., Alves, T.C., Petersen, K.F., Rothman, D.L., Kibbey, R.G., and Shulman, G.I. (2016). Propionate increases hepatic pyruvate cycling and anaplerosis and alters mitochondrial metabolism. J. Biol. Chem. *291*, 12161–12170.

Petersen, K.F., Blair, J.B., and Shulman, G.I. (1995). Triiodothyronine treatment increases substrate cycling between pyruvate carboxylase and malic enzyme in perfused rat liver. Metab. Clin. Exp. *44*, 1380–1383.

Petersen, M.C., Vatner, D.F., and Shulman, G.I. (2017). Regulation of hepatic glucose metabolism in health and disease. Nat. Rev. Endocrinol. *13*, 572–587.

Polyzos, S.A., Kountouras, J., and Mantzoros, C.S. (2019). Obesity and nonalcoholic fatty liver disease: from pathophysiology to therapeutics. Metabolism *92*, 82–97.

Previs, S.F., and Kelley, D.E. (2015). Tracer-based assessments of hepatic anaplerotic and TCA cycle flux: practicality, stoichiometry, and hidden assumptions. Am. J. Physiol. Endocrinol. Metab. *309*, E727–E735.

Quek, L.-E., Dietmair, S., Krömer, J.O., and Nielsen, L.K. (2010). Metabolic flux analysis in mammalian cell culture. Metab. Eng. *12*, 161–171.

Reisz, J.A., and D'Alessandro, A. (2017). Measurement of metabolic fluxes using stable isotope tracers in whole animals and human

patients. Curr. Opin. Clin. Nutr. Metab. Care *20*, 366–374.

Reznik, E., Christodoulou, D., Goldford, J.E., Briars, E., Sauer, U., Segrè, D., and Noor, E. (2017). Genome-scale Architecture of small molecule regulatory networks and the fundamental trade-off between regulation and enzymatic activity. Cell Rep. *20*, 2666–2677.

Roden, M., and Shulman, G.I. (2019). The integrative biology of type 2 diabetes. Nature *576*, 51–60.

Ros, S., et al. (2009). Control of liver glycogen synthase activity and intracellular distribution by phosphorylation. Journal of Biological Chemistry *284* (10), 6370–6378. https://doi.org/10.1074/jbc.M808576200.

Saa, P., and Nielsen, L.K. (2015). A general framework for thermodynamically consistent parameterization and efficient sampling of enzymatic reactions. PLoS Comput. Biol. *11*, 1–25.

Saa, P.A., and Nielsen, L.K. (2016). Construction of feasible and accurate kinetic models of metabolism: a Bayesian approach. Sci. Rep. *6*, 29635.

Saa, P.A., and Nielsen, L.K. (2017). Formulation, construction and analysis of kinetic models of metabolism: a review of modelling frameworks. Biotechnol. Adv. *35*, 981–1003.

Samuel, V.T., Beddow, S.A., Iwasaki, T., Zhang, X.M., Chu, X., Still, C.D., Gerhard, G.S., and Shulman, G.I. (2009). Fasting hyperglycemia is not associated with increased expression of PEPCK or G6Pc in patients with type 2 diabetes. Proc. Natl. Acad. Sci. U S A *106*, 12121–12126.

Satapati, S., Sunny, N.E., Kucejova, B., Fu, X., He, T.T., Méndez-Lucas, A., Shelton, J.M., Perales, J.C., Browning, J.D., and Burgess, S.C. (2012). Elevated TCA cycle function in the pathology of diet-induced hepatic insulin resistance and fatty liver. J. Lipid Res. *53*, 1080–1092.

Smallbone, K., Messiha, H.L., Carroll, K.M., Winder, C.L., Malys, N., Dunn, W.B., Murabito, E., Swainston, N., Dada, J.O., Khan, F., et al. (2013). A model of yeast glycolysis based on a consistent kinetic characterisation of all its enzymes. FEBS Lett. *587*, 2832–2841.

Soga, T., and Heiger, D.N. (2000). Amino acid analysis by capillary electrophoresis electrospray ionization mass spectrometry. Anal. Chem. *72*, 1236–1241.

Soga, T., Baran, R., Suematsu, M., Ueno, Y., Ikeda, S., Sakurakawa, T., Kakazu, Y., Ishikawa, T., Robert, M., Nishioka, T., et al. (2006). Differential metabolomics reveals ophthalmic acid as an oxidative stress biomarker indicating hepatic glutathione consumption. J. Biol. Chem. *281*, 16768–16776.

Soga, T., Igarashi, K., Ito, C., Mizobuchi, K., Zimmermann, H.P., and Tomita, M. (2009). Metabolomic profiling of anionic metabolites by capillary electrophoresis mass spectrometry. Anal. Chem. *81*, 6165–6174.

Soltis, A.R., Kennedy, N.J., Xin, X., Zhou, F., Ficarro, S.B., Yap, Y.S., Matthews, B.J., Lauffenburger, D.A., White, F.M., Marto, J.A., et al. (2017). Hepatic dysfunction caused by consumption of a high-fat diet. Cell Rep. *21*, 3317–3328.

Srivastava, A., Kowalski, G.M., Callahan, D.L., Meikle, P.J., and Creek, D.J. (2016). Strategies for extending metabolomics studies with stable isotope labelling and fluxomics. Metabolites *6*, 32.

Sugimoto, M., Wong, D.T., Hirayama, A., Soga, T., and Tomita, M. (2010). Capillary electrophoresis mass spectrometry-based saliva metabolomics identified oral, breast and pancreatic cancer-specific profiles. Metabolomics *6*, 78–95.

Sunny, N.E., Parks, E.J., Browning, J.D., and Burgess, S.C. (2011). Excessive hepatic mitochondrial TCA cycle and gluconeogenesis in humans with nonalcoholic fatty liver disease. Cell Metab. *14*, 804–810.

Surinova, S., Hüttenhain, R., Chang, C.-Y., Espona, L., Vitek, O., and Aebersold, R. (2013). Automated selected reaction monitoring data analysis workflow for large-scale targeted proteomic studies. Nat. Protoc. *8*, 1602–1619.

Teusink, B., Passarge, J., Reijenga, C.A., Esgalhado, E., Van Der Weijden, C.C., Schepper, M., Walsh, M.C., Bakker, B.M., Van Dam, K., Westerhoff, H.V., et al. (2000). Can yeast glycolysis be understood terms of vitro kinetics of the constituent enzymes? Testing biochemistry. Eur. J. Biochem. *267*, 5313–5329.

Tran, L.M., Rizk, M.L., and Liao, J.C. (2008). Ensemble modeling of metabolic networks. Biophys. J. *95*, 5606–5617.

Trapnell, C., Pachter, L., and Salzberg, S.L. (2009). TopHat: discovering splice junctions with RNA-Seq. Bioinformatics *25*, 1105–1111.

Trapnell, C., Roberts, A., Goff, L., Pertea, G., Kim, D., Kelley, D.R., Pimentel, H., Salzberg, S.L., Rinn, J.L., and Pachter, L. (2012). Differential gene and transcript expression analysis of RNA-seq experiments with topHat and cufflinks. Nat. Protoc. *7*, 562–578.

Turner, S.M., Linfoot, P.A., Neese, R.A., and Hellerstein, M.K. (2005). Sources of plasma glucose and liver glycogen in fasted ob/ob mice. Acta Diabetol. *42*, 187–193.

Wang, L., Birol, I., and Hatzimanikatis, V. (2004). Metabolic control analysis under uncertainty: framework development and case studies. Biophys. J. *87*, 3750–3763.

Wang, Y., Kwon, H., Su, X., and Wondisford, F.E. (2020). Glycerol not lactate is the major net carbon source for gluconeogenesis in mice during both short and prolonged fasting. Mol. Metab. *31*, 36–44.

Wiley, H.S. (2011). Integrating multiple types of data for signaling research: challenges and opportunities. Sci. Signal. *4*, pe9.

Yugi, K., Kubota, H., Toyoshima, Y., Noguchi, R., Kawata, K., Komori, Y., Uda, S., Kunida, K., Tomizawa, Y., Funato, Y., et al. (2014). Reconstruction of insulin signal flow from phosphoproteome and metabolome data. Cell Rep. *8*, 1171–1183.

Yugi, K., Kubota, H., Hatano, A., and Kuroda, S. (2016). Trans-omics: how to reconstruct biochemical networks across multiple "omic" layers. Trends Biotechnol. *34*, 276–290.

Yugi, K., Ohno, S., Krycer, J.R., James, D.E., and Kuroda, S. (2019). Rate-oriented trans-omics: integration of multiple omic data on the basis of reaction kinetics. Curr. Opin. Syst. Biol. *15*, 109–120.

Please cite this article in press as: Uematsu et al., Multi-omics-based label-free metabolic flux inference reveals obesity-associated dysregulatory mechanisms in liver glucose metabolism, iScience (2022), https://doi.org/10.1016/j.isci.2022.103787

CellPress
OPEN ACCESS

STAR★METHODS

KEY RESOURCES TABLE

REAGENT or RESOURCE	SOURCE	IDENTIFIER
Deposited data		
Metabolomic data	This study	N/A
Proteomic data	This study	JPOST: JPST000147 JPOST: JPST000148 JPOST: JPST001222
Transcriptomic data in WT and *ob/ob* mice in the fasting state (all samples) and after oral glucose administration (n = 5)	Kokaji et al. (2020)	DRA: DRA008416
Transcriptomic data in WT and *ob/ob* mice after oral glucose administration (n = 7)	This study	DRA: DRA012292
Experimental models: Organisms/strains		
Mouse: C57BL/6J	Japan SLC Inc.	C57BL/6JJmsSlc
Mouse: *ob/ob*	Japan SLC Inc.	C57BL/6JHamSlc-ob/ob
Software and algorithms		
MATLAB R2019a	MathWorks	https://jp.mathworks.com/products/matlab.html
Docker 20.10.6	Merkel (2014)	https://www.docker.com/
R 3.6.1	R Core Team	https://www.r-project.org
RStan 2.19.2	Stan Development Team	http://mc-stan.org/
BioModels	Le Novère et al. (2006)	https://www.ebi.ac.uk/biomodels/
Other		
Omics-Based Metabolic Flux Estimation without Labeling for Extended Trans-omic Analysis (OMELET)	This study	https://github.com/usa0ri/OMELET
Docker image for RStan	This study	https://hub.docker.com/repository/docker/saori/rstan
Kinetic model of yeast glycolysis	Smallbone et al. (2013) Messiha et al. (2014)	BIOMD0000000503
Kinetic model of hepatocyte glucose metabolism	Marín-Hernández et al. (2020)	N/A

RESOURCE AVAILABILITY

Lead contact

Further information and requests for resources and reagents should be directed to and will be fulfilled by the Lead Contact, Shinya Kuropda (skuroda@bs.s.u-tokyo.ac.jp).

Materials availability

This study did not generate new unique reagents.

Data and code availability

- The accession number for the data of proteome analysis reported in this paper is the ProteomeXchange Consortium (http://proteomecentral.proteomexchange.org) via the JPOST partner repository: JPST000147, JPST000148, and JPST001222. Sequence data used in this study have been deposited in the DNA Data Bank of Japan Sequence Read Archive (DRA) (www.ddbj.nig.ac.jp/): DRA008416, DRA012292.

- The MATLAB and R code for OMELET is available at GitHub (https://github.com/usa0ri/OMELET). An image for Docker container that include RStan and R software to perform OMELET is available at DockerHub Registry (https://hub.docker.com/repository/docker/saori/rstan).
- The datasets generated during this study are in the published article.

EXPERIMENTAL MODEL AND SUBJECT DETAILS

Animals

We used the mouse liver samples obtained simultaneously with those previously published (Egami et al., 2021; Kokaji et al., 2020). Briefly, 10-week-old male C57BL/6J wild-type and *ob*/*ob* mice (Japan SLC, Inc., Shizuoka, Japan) were overnight (16 hours) fasted or administrated 2 g/kg body weight of glucose orally after overnight fasting. The mice before or four-hour after glucose loading were sacrificed by cervical dislocation and the whole or left lobe of the liver was dissected and immediately frozen in liquid nitrogen. The frozen liver was pulverized with dry ice to a fine powder with a blender and separated into tubes for transcriptomic, proteomic, and metabolomic measurements. Note that all the omics data was simultaneously measured from the same individual mice. All the mouse experiments were performed according to protocols approved by the animal ethics committee of The University of Tokyo.

We had mice under four conditions: WT mice in the fasting state (n = 11), *ob*/*ob* mice in the fasting state (n = 12), WT mice after oral glucose administration (n = 12), and *ob*/*ob* mice after oral glucose administration (n = 12). The metabolomic data of five samples in each condition were reported in our previous studies (Egami et al., 2021; Kokaji et al., 2020). We obtained the metabolomic data from all the samples in this study. The transcriptomic data from all the samples in the fasting state and five after oral glucose administration were reported in our previous studies. We obtained the transcriptomic data from seven samples after oral glucose administration in this study.

METHOD DETAILS

Metabolic network for glucose metabolism in mice

A metabolic network for glucose metabolism in mice was constructed to infer metabolic fluxes and calculate the contributions of regulators to changes in metabolic flux between conditions. The network consists of 35 metabolites and 22 reactions (Table S1) in gluconeogenesis, glycogenolysis, lactate and alanine metabolism, and the TCA cycle (Figure 2).

We included isoforms whose gene expression levels were high in the liver in the metabolic network. Most of the cytosolic enzymes had one dominant isoform and the amounts of transcripts of other isoforms were much lower under all the conditions we analyzed, suggesting that other isoforms would not modify the enzyme activity carried by the dominant isoforms.

The liver produces glucose through the gluconeogenesis and consumes glucose through glycolysis. The gluconeogenesis in liver includes reactions catalyzed by glucose 6-phosphatase (G6PC) and fructose-bisphosphatase 1 (FBPase), while the glycolysis includes reactions by glucokinase (GK) and phosphofructokinase (liver type) (PFKL). Assuming that the metabolic flux through GK and PFKL were negligible in livers of WT and *ob*/*ob* mice in all the conditions, we included G6PC and FBPase in the metabolic network but not included GK and PFKL. This is supported by several studies showing that the glucose production was more dominant than the glucose consumption in livers of overnight fasting WT mice (Burgess et al., 2005; Hasenour et al., 2015, 2020; Satapati et al., 2012; Wang et al., 2020) and *ob*/*ob* mice (Turner et al., 2005). We also assumed that glucose consumption and metabolic fluxes through GK and PFKL are negligible four hours after oral glucose administration, supported by previous studies using rats (Jin et al., 2003). Although we did not find any studies to support the glucose production in *ob*/*ob* mice four hours after oral glucose administration, *ob*/*ob* mice after oral glucose administration in this study showed similar temporal changes in blood glucose and insulin (Figures S1A and S1B) to WTWT mice. In addition, PFKL enzyme was not quantified at the protein level because its amounts were smaller than other enzymes in the glucose metabolism (Matsumoto et al., 2017). GK enzyme was quantified at the protein level but its substrate, free glucose, was not measured. Therefore, we included G6PC and FBPase in the metabolic network but not included GK and PFKL reactions. This also reduces the complexity of the metabolic model and computational cost for the metabolic flux estimation.

Please cite this article in press as: Uematsu et al., Multi-omics-based label-free metabolic flux inference reveals obesity-associated dysregulatory mechanisms in liver glucose metabolism, iScience (2022), https://doi.org/10.1016/j.isci.2022.103787

Although glycogen phosphorylase and glycogen synthase are important to analyze glycogen degradation and synthesis, we did not include these reactions in our metabolic network because the amounts of these enzymes were not measured. The reason why we did not include glycogen phosphorylase and glycogen synthase is that the regulation of glycogen metabolism is so complex that OMELET would not precisely infer the metabolic flux through glycogen phosphorylase and glycogen synthase from the amounts of these enzymes and associating metabolites. Phosphorylation and subcellular localization of enzymes and hormones play important roles in regulations of glycogen metabolism in the mammalian liver ((Ros, 2009) Han et al., 2016), which makes the modeling very complex. In addition, we did not examine enzyme activities (Vmax or kcat) and assumed that kcat is constant. This assumption would be not the case with glycogen phosphorylase and glycogen synthase. For these reasons, we anticipated that it would be difficult to infer metabolic flux and its regulation even if the amounts of glycogen phosphorylase and glycogen synthase are available. Therefore, we considered only PGM to express the net glycogen metabolic flux.

Glycogen levels increased after oral glucose administration in both WT and *ob*/*ob* mice (Figure 2); however, it is unclear whether glycogen degradation or synthesis is dominant at four hours after oral glucose administration. Therefore, we did not fix the direction of PGM reaction either toward glycogen synthesis or degradation.

Pyruvate dehydrogenase (PDH), converting pyruvate to acetyl-CoA, was not included in the metabolic network because several studies showed that the metabolic flux through PDH was small (~5%) relative to those through the TCA cycle in WT mice in the fasting state (Perry et al., 2016). Malic enzyme (ME), converting malate to pyruvate, was not considered because ME inhibitor did not affect the metabolic flux producing pyruvate in fasting rodent models (Hasenour et al., 2020; Perry et al., 2016; Petersen et al., 1995), suggesting the small contribution of ME to the metabolic flux.

Cytosolic and mitochondrial compartments were not considered for simplification and averaged metabolic fluxes as a single compartment were inferred in this study. Malate dehydrogenase (Mdh) has cytosolic (Mdh1) and mitochondrial (Mdh2) isoforms, but we only considered Mdh2 as a part of reactions in the TCA cycle for simplification.

OMELET is based on a Bayesian method and evaluates likelihood of the enzyme and transcript amounts based on measured data (see the following sections), but we did not use all enzymes and transcripts in the metabolic network for evaluation of the likelihood. Glucose 6-phosphatase was not used for evaluation of the likelihood because it could not be quantified at the protein level. This was because unique peptides for mouse glucose 6-phosphatase were not identified in data-dependent acquisition (DDA). Reactions from citrate to succinate including aconitase (ACO), isocitrate dehydrogenase (IDH), and alpha-ketoglutarate dehydrogenase (OGDH) were not used to evaluate the likelihood of their enzymes because the amounts of their substrates and products were not measured. Since reaction kinetics are not described for ACO, IDH, and OGDH in OMELET, we did not include the NADH as a product inhibitor of these enzymes. Note that production of NADH from ACO to OGDH is included in the stoichiometric matrix of the metabolic network. Bicarbonate in PC and CO_2 in PEPCK were not included because we assumed that their amounts are constant across the conditions and do not affect changes in metabolic flux between conditions. Fructose 2,6-bisphosphate was not included as an allosteric inhibitor of FBPase because its amount was not measured in our metabolomic analysis. Reactions in which $NADP^+$ and NADPH participate were not described in reaction kinetics in OMELET.

Algorithm of OMELET

We first review a framework of Bayesian inference. Statistical model consists of a likelihood, representing a probability of the observed data $\boldsymbol{z}$ at a given parameter values $\boldsymbol{\theta}$, and a prior distribution for $\boldsymbol{\theta}$, denoting a probability distribution of each parameter reflecting the feasible assumptions and prior knowledges. Bayes' theorem calculates the renormalized product of the likelihood $p(\boldsymbol{z}|\boldsymbol{\theta})$ and the prior distribution $p(\boldsymbol{\theta})$,

$$p(\boldsymbol{\theta}|\boldsymbol{z}) \propto p(\boldsymbol{z}|\boldsymbol{\theta})p(\boldsymbol{\theta})$$

to produce the posterior parameter distribution $p(\boldsymbol{\theta}|\boldsymbol{z})$, a probability of the parameters taking the values given the observed data. The posterior distribution is obtained by updating the parameter values following the prior distributions toward better fittings to the observed data evaluated in likelihood. The definition of the prior distribution is critical especially when the sample size is small whereas sufficient samples make its

effects on posterior parameter distribution decreases to get closer to maximal likelihood estimation. One may assume additional parameters for prior distributions, which can be achieved by defining hyperparameters $\boldsymbol{\eta}$,

$$p(\boldsymbol{\theta}, \boldsymbol{\eta}|\boldsymbol{z}) \propto p(\boldsymbol{z}|\boldsymbol{\theta}) p(\boldsymbol{\theta}|\boldsymbol{\eta}) p(\boldsymbol{\eta})$$

to introduce a hierarchical structure in prior distributions. Furthermore, Bayesian regression uses the additional observed data $\boldsymbol{w}$ as explanatory variables to calculate posterior distributions defined as

$$p(\boldsymbol{\theta}, \boldsymbol{\eta}|\boldsymbol{z}, \boldsymbol{w}) \propto p(\boldsymbol{z}|\boldsymbol{\theta}, \boldsymbol{w}) p(\boldsymbol{\theta}|\boldsymbol{\eta}) p(\boldsymbol{\eta}).$$

In Omics-based Metabolic flux Estimation without Labeling for Extended Trans-omic analysis (OMELET), observed data $\boldsymbol{z}$ is the experimental data of the amounts of enzymes and transcripts from the same samples obtained from multiple conditions. The observed data $\boldsymbol{w}$ as explanatory variables is the experimental data of the amounts of metabolites. Parameters $\boldsymbol{\theta}$ include metabolic fluxes in each condition, elasticity coefficients in linlog kinetics and mRNA-to-protein ratios. The prior $p(\boldsymbol{\theta})$ is defined for all the parameters, and the hyperprior $p(\boldsymbol{\eta})$ is defined only for metabolic fluxes, which has hyperparameters $\boldsymbol{\eta}$ to obtain a steady-state metabolic flux distribution based on the reactions of the metabolic network of interest. The likelihood $p(\boldsymbol{z}|\boldsymbol{\theta})$, which describes the relationship between the experimental data and the parameters, is the product of the probability of the measured amounts of enzymes given the parameters and the probability of the measured amounts of transcripts given the parameters.

We start from defining the prior and hyperprior for metabolic fluxes as multivariable normal distribution in each condition $l = 1, 2, \ldots, g$. The metabolite concentration $\boldsymbol{x}_l$ and metabolic fluxes $\boldsymbol{v}_l$ describes a system of mass balances around each metabolite in the form

$$\dot{\boldsymbol{x}}_l = \boldsymbol{S}\boldsymbol{v}_l \qquad \text{(Equation 1)}$$

for r' reactions and m metabolites, where $\boldsymbol{S}$ denotes the stoichiometric matrix that links metabolites to their reactions via stoichiometry. Note that this stoichiometric matrix is based on the open-formed metabolic network that is transformed by removing rows for the metabolites that participated in transporting reaction across the system boundary, resulting in $m<r'$. The vector of the time derivative for metabolites $\dot{\boldsymbol{x}}_l$ around steady state is assumed to follow m-dimensional multivariate normal distribution

$$\dot{\boldsymbol{x}}_l \sim \mathcal{N}\left(0, {\boldsymbol{\Sigma}_l}^{\dot{x}}\right) \qquad \text{(Equation 2)}$$

with diagonal covariance matrix ${\boldsymbol{\Sigma}_l}^{\dot{x}} = \mathrm{diag}({\boldsymbol{\sigma}_l}^{\dot{x}})^2$. ${\boldsymbol{\sigma}_l}^{\dot{x}}$ represents the extent of relaxation from the steady state and is defined later based on the influx and efflux around each metabolite. The number of variables that need to be specified to calculate a steady-state fluxes in (Equation 1) is $f = r' - \mathrm{rank}(\boldsymbol{S})$. Let us denote the vectors of independent and dependent flux variables $\boldsymbol{u}_l$ and $\boldsymbol{v}_l^d$ of length f and rank($\boldsymbol{S}$), respectively. Since dependent flux variables can be directly computed as linear combination of independent flux variables, we have only to estimate independent flux as hyperparameter to obtain the full metabolic fluxes. Here the vector of independent flux was assumed to follow the multi-dimensional normal distribution

$$p\left(\boldsymbol{u}_l|\boldsymbol{\mu}_l^u\right) = \mathcal{N}\left(\boldsymbol{u}_l|\boldsymbol{\mu}_l^u, \boldsymbol{\Sigma}_l^u\right) \qquad \text{(Equation 3)}$$

with mean $\boldsymbol{\mu}_l^u$ and diagonal covariance matrix $\boldsymbol{\Sigma}_l^u = \mathrm{diag}(\boldsymbol{\sigma}_l^u)^2$. The deviations of independent fluxes were determined as $\boldsymbol{\sigma}_l^u = c^u \boldsymbol{\mu}_l^u$ with a fixed coefficient of variance c^u. The relation between independent and dependent flux variables can be obtained via decomposition of the full flux vector into the vectors of independent and dependent flux, and the (Equation 1) can be expressed as

$$\dot{\boldsymbol{x}}_l = \begin{bmatrix} \boldsymbol{S}^d & \boldsymbol{S}^u \end{bmatrix} \begin{bmatrix} \boldsymbol{v}_l^d \\ \boldsymbol{u}_l \end{bmatrix} = \boldsymbol{S}^d \boldsymbol{v}_l^d + \boldsymbol{S}^u \boldsymbol{u}_l \qquad \text{(Equation 4)}$$

where $m\times\mathrm{rank}(\boldsymbol{S})$ matrix $\boldsymbol{S}^d$ and $m\times f$ matrix $\boldsymbol{S}^u$ contain columns corresponding to dependent and independent flux variables, respectively. When $\boldsymbol{S}^d$ is regular with $m = \mathrm{rank}(\boldsymbol{S})$ and $\det(\boldsymbol{S}^d) \neq 0$, the full flux vector is directly computed as

$$\boldsymbol{v}_l = \begin{bmatrix} \boldsymbol{v}_l^d \\ \boldsymbol{u}_l \end{bmatrix} = \begin{bmatrix} \left(\boldsymbol{S}^d\right)^{-1} \left(\dot{\boldsymbol{x}}_l - \boldsymbol{S}^u \boldsymbol{u}_l\right) \\ \boldsymbol{u}_l \end{bmatrix} = \begin{bmatrix} -\left(\boldsymbol{S}^d\right)^{-1} \boldsymbol{S}^u \\ \boldsymbol{I}_{r-m} \end{bmatrix} \boldsymbol{u}_l + \begin{bmatrix} \left(\boldsymbol{S}^d\right)^{-1} \\ 0 \end{bmatrix} \dot{\boldsymbol{x}}_l = \boldsymbol{W}^u \boldsymbol{u}_l + \boldsymbol{W}^{\dot{x}} \dot{\boldsymbol{x}}_l \qquad \text{(Equation 5)}$$

with transformation matrices $\boldsymbol{W}^u$ and $\boldsymbol{W}^{\dot{x}}$ defined based on the inverse of $\boldsymbol{S}^d$. Here we just considered the metabolic pathways in which the stoichiometric matrix $\boldsymbol{S}^d$ was regular, and in other words the following

situation was not considered because the full metabolic fluxes could not be computed from independent flux variables: $r' < m$ or linearly dependent rows in $\boldsymbol{S}$ resulting in rank($\boldsymbol{S}$)$<m$. We avoided these conditions by appropriate definition of the target metabolic pathway and stoichiometric matrix.

Now we obtain the prior distribution of the full metabolic fluxes from (Equation 5). Since linear combination of normal random variables is also normal random variables, the vector of full metabolic flux follows the r'-dimensional normal distribution

$$p(\boldsymbol{v}_l|\boldsymbol{u}_l) = \mathcal{N}\left(\boldsymbol{v}_l\middle|\boldsymbol{\mu}_l^{\boldsymbol{v}}, \boldsymbol{\Sigma}_l^{\boldsymbol{v}}\right) \quad \text{(Equation 6)}$$

with mean $\boldsymbol{\mu}_l^{\boldsymbol{v}} = \boldsymbol{W}^{\boldsymbol{u}}\boldsymbol{\mu}_l^{\boldsymbol{u}}$ and covariance matrix $\boldsymbol{\Sigma}_l^{\boldsymbol{v}} = \boldsymbol{W}^{\boldsymbol{u}}\boldsymbol{\Sigma}_l^{\boldsymbol{u}}(\boldsymbol{W}^{\boldsymbol{u}})^\top + \boldsymbol{W}^{\dot{\boldsymbol{x}}}\boldsymbol{\Sigma}_l^{\dot{\boldsymbol{x}}}(\boldsymbol{W}^{\dot{\boldsymbol{x}}})^\top$. The diagonal covariance matrix $\boldsymbol{\Sigma}_l^{\dot{\boldsymbol{x}}}$ represents the variances around prior metabolite changes. In strict steady state, the prior for metabolite change becomes Dirac's delta function at zero by increasing the variances, we can relax the steady-state assumption on individual metabolites and encode allowance for accumulations or depletions of them. The squared diagonal element $\boldsymbol{\sigma}_l^{\dot{\boldsymbol{x}}}$ was obtained from the mean of the prior distribution of metabolic flux as

$$\boldsymbol{\sigma}_l^{\dot{\boldsymbol{x}}} = \frac{c^{\dot{\boldsymbol{x}}}}{2}\left(\boldsymbol{S}^+\boldsymbol{\mu}_l^{\boldsymbol{v}} + \boldsymbol{S}^-\boldsymbol{\mu}_l^{\boldsymbol{v}}\right), \quad \text{(Equation 7)}$$

with a fixed coefficient of variance $c^{\dot{\boldsymbol{x}}}$ by defining production and consumption stoichiometric matrices as,

$$S^+ = \frac{1}{2}(\mathrm{abs}(\boldsymbol{S}) + \boldsymbol{S}), \quad S^- = \frac{1}{2}(\mathrm{abs}(\boldsymbol{S}) - \boldsymbol{S}), \quad \text{(Equation 8)}$$

where abs($\boldsymbol{S}$) is the matrix of absolute values of the corresponding entries of $\boldsymbol{S}$. Note that the entries of the matrix $\boldsymbol{S}^+$ corresponds to the number of molecules of metabolite produced by the reaction. Conversely, each entry of the matrix $\boldsymbol{S}^-$ give the number of molecules of metabolite consumed by the reaction.

Next, we define the likelihood of the measured amounts of enzymes given parameters and prior for elasticity coefficients based on linlog kinetics. Since the experimental data of the amounts of metabolites and enzymes is usually not available for all reactions in the metabolic network, the likelihood was calculated for a subset of the reactions. We consider the metabolic flux through the subset of the reactions $R \subseteq R' = \{1, 2, \ldots, r'\}$, where R consists of r reactions. For each sample $k = 1, 2, \ldots, n_j$ under condition l ($l = 1, 2, \ldots, g$), the amounts of metabolites $\boldsymbol{x}_{kl}$ (a $m\times1$ vector) and the amounts of enzymes $\boldsymbol{e}_{kl}$ (a $r\times1$ vector) are obtained after normalizing by the average amounts across all the conditions. In the linlog kinetics framework, the metabolic flux through reaction $j \in R$ ($\hat{v}_{jkl}$) is expressed as

$$\hat{v}_{jkl} = v_j^0 e_{jkl}\left(1 + \varepsilon_j^\top \ln \boldsymbol{x}_{kl}\right), \quad \text{(Equation 9)}$$

where v_j^0 is the metabolic flux in the reference state, and ε_j is the $m\times1$ vector of elasticity coefficients. v_j^0 is defined as the mean of the prior metabolic flux values across conditions as $v_j^0 = 1/g\sum_{l=1}^{g}\mu_{jl}^{\boldsymbol{v}}$ where $\mu_{jl}^{\boldsymbol{v}}$ is a prior mean of the metabolic flux v_{jl}. ε_{ji} describes the effect of changes of the amounts of metabolites x_i on the metabolic flux v_j, and is positive if metabolite i is a substrate or an allosteric activator for reaction j, while negative if the metabolite is a product or an allosteric inhibitor. If metabolite i does not directly participate in reaction j, the value of ε_{ji} equals to zero. According to (Equation 9) the amount of the enzyme is calculated using the inferred metabolic flux v_{jl}. Here, the amount of the enzyme in each sample e_{jkl} is assumed to follow the normal distribution around the estimated value $\hat{e}_{jkl}$, and we obtain the likelihood of the measured amount of the enzyme given parameters as

$$\begin{aligned} p\left(e_{jkl}\middle|\boldsymbol{x}_{kl}, v_{jl}, \varepsilon_j, \widehat{\sigma^e}\right) &= \mathcal{N}\left(e_{jkl}\middle|\hat{e}_{jkl}, (\widehat{\sigma^e})^2\right), \\ \hat{e}_{jkl} &= \frac{v_{jl}}{v_j^0}\frac{1}{1+\varepsilon_j^\top \ln \boldsymbol{x}_{kl}}, \end{aligned} \quad \text{(Equation 10)}$$

where v_{jl} is the inferred metabolic flux of reaction j. For simplicity, the variance of the error term $\widehat{\sigma^e}$ is set to the same values in all the reactions, samples, and conditions. We placed half-Cauchy priors with scale 0.5 on $\widehat{\sigma^e}$, set as a weakly informative prior distribution given that $\widehat{\sigma^e}$ was expected to be less than one.

Elasticity coefficients are likely not to significantly deviate from the range between -1 and 1 theoretically (Kacser and Burns, 1995), and are likely to be positive for substrates and allosteric activators whereas

negative for products and allosteric inhibitors. This property generates prior distributions for elasticity coefficients as

$$p(\varepsilon_{ji}) = \begin{cases} \mathcal{H}(\varepsilon_{ji}|1) \text{ if metabolite } i \text{ is substrate} \\ \text{or allosteric activator in reaction } j \\ \mathcal{H}(-\varepsilon_{ji}|1) \text{ if metabolite i is product} \\ \textit{or allosteric inhibitor in reaction } j \\ \delta(\varepsilon_{ji}|0) \text{ others} \end{cases} \quad \text{(Equation 11)}$$

$$\mathcal{H}(x|\sigma) = \frac{\sqrt{2}}{\sigma\sqrt{\pi}} \exp\left(-\frac{x^2}{2\sigma^2}\right),\ x \in [0, +\infty)s$$

$$\delta(x|\mu) = \lim_{\sigma \to 0} \frac{1}{\sqrt{2\pi\sigma^2}} \exp\left(-\frac{(x-\mu)^2}{2\sigma^2}\right),\ x \in (-\infty, +\infty)$$

where $\mathcal{H}(x|\sigma)$ indicates half-normal distribution with variance σ, and $\delta(x|\mu)$ indicates Dirac's delta function equal to zero everywhere except for μ.

Theoretically, the elasticity coefficient in linlog kinetics indicates the degree of saturation of the enzyme with a particular metabolite, and can qualitatively capture the saturation of individual enzymes with their regulators (Childs et al., 2015; Wang et al., 2004). The greater the absolute value of elasticity with its metabolite, the less saturated the enzyme catalyzing the reaction is with the metabolite. The assumption in OMELET that elasticity coefficients are likely to be close to zero is consistent with the distribution of experimentally calculated elasticity coefficients of more than 4,000 reactions in *E. coli* (Reznik et al., 2017).

The amounts of enzymes are explained in the context of not only metabolic flux but also of protein turnover. Here we define the likelihood of the measured amounts of transcripts given parameters and priors for mRNA-to-protein ratio β_{ij}. For each sample $k = 1, 2, \ldots, n_j$ under condition l ($l = 1, 2, \ldots, g$), the estimated amounts of enzymes $\hat{\mathbf{e}}_{kl}$ and the corresponding amounts of transcripts $\hat{\mathbf{t}}_{kl}$ represents the enzyme change rate $\dot{\boldsymbol{e}}_{kl}$ as

$$\dot{\boldsymbol{e}}_{kl} = \left(\boldsymbol{k}_l^+\right)^\top \hat{\mathbf{t}}_{kl} - \left(\boldsymbol{k}_l^-\right)^\top \hat{\mathbf{e}}_{kl}, \quad \text{(Equation 12)}$$

where $\boldsymbol{k}_l^+$ and $\boldsymbol{k}_l^-$ are $r \times 1$ vectors of kinetic parameters for protein synthesis and degradation, respectively. Assuming the amounts of enzymes as stable within the observed time intervals, the amounts of enzymes and transcripts have a linear relationship and we obtain the likelihood of the measured amount of the transcript given parameters as,

$$p\left(t_{jkl}|\hat{e}_{jkl}, \beta_{jl}, \widehat{\sigma^t}\right) = \mathcal{N}\left(t_{jkl}\middle|\hat{t}_{jkl}, \left(\widehat{\sigma^t}\right)^2\right),$$
$$\hat{t}_{jkl} = \frac{1}{\beta_{jl}}\hat{e}_{jkl}, \quad \text{(Equation 13)}$$

using mRNA-to-protein ratio $\beta_{jl} = k_{jl}^+ / k_{jl}^-$ and the estimated amount of enzyme $\hat{e}_{jkl}$ in each sample defined in (Equation 10). The parameter to determine the variance of the error term $\widehat{\sigma^t}$ is simplified as the common values in all the reactions, samples, and conditions. We placed half-Cauchy priors with scale 0.5 on $\widehat{\sigma^t}$. Given that there is a high correlation between copy numbers of RNA and protein especially in the glucose metabolism (Matsumoto et al., 2017), the mRNA-to-protein ratio β_{jl} is expected to be close to one when the amounts of enzymes and transcripts are normalized to their averages. Therefore, the prior distribution for β_{jl} can be described by

$$p\left(\beta_{jl}|\sigma_l^\beta\right) = \mathcal{N}\left(\beta_{jl}\middle|1, \left(\sigma_l^\beta\right)^2\right) \quad \text{(Equation 14)}$$

with error term defined by σ_l^β in each condition. We placed half-Cauchy priors with scale 0.5 on σ_l^β.

Combining the likelihood with the priors based on linlog kinetics (Equations 6, 10 and 11, and Table S7) and protein turnover (Equations 13 and 14, and Table S7), the joint posterior distribution is given by

$$\begin{aligned} & p(\boldsymbol{v}, \varepsilon, \boldsymbol{\beta}, \widehat{\sigma^e}, \widehat{\sigma^t} | \boldsymbol{e}, \boldsymbol{x}, \boldsymbol{t}, c^u, c^{\dot{x}}, S) \\ \propto & p(\boldsymbol{e}, \boldsymbol{t} | \boldsymbol{x}, \boldsymbol{v}, \varepsilon, \widehat{\sigma^e}, \boldsymbol{\beta}, \widehat{\sigma^t}) p(\boldsymbol{v} | \boldsymbol{u}, c^{\dot{x}}, S) p(\boldsymbol{u} | \boldsymbol{\mu}^u, c^u) p(\varepsilon) p(\boldsymbol{\beta}) p(\widehat{\sigma^e}) p(\widehat{\sigma^t}), \\ & p(\boldsymbol{e}, \boldsymbol{t} | \boldsymbol{x}, \boldsymbol{v}, \varepsilon, \widehat{\sigma^e}, \boldsymbol{\beta}, \widehat{\sigma^t}) = p(\boldsymbol{e} | \boldsymbol{x}, \boldsymbol{v}, \varepsilon, \widehat{\sigma^e}) p(\boldsymbol{t} | \boldsymbol{x}, \boldsymbol{v}, \varepsilon, \boldsymbol{\beta}, \widehat{\sigma^t}). \end{aligned} \quad \text{(Equation 15)}$$

where $p(\boldsymbol{e}, \boldsymbol{t} | \boldsymbol{x}, \boldsymbol{v}, \varepsilon, \widehat{\sigma^e}, \boldsymbol{\beta}, \widehat{\sigma^t})$ is the likelihood of the measured amounts of enzymes based on linlog kinetics combined with the likelihood of the measured amounts of transcripts based on protein turnover, $p(\boldsymbol{v} | \boldsymbol{u}, c^{\dot{x}}, S)$ is the prior distribution for metabolic flux $\boldsymbol{v}$, $p(\boldsymbol{u} | \boldsymbol{\mu}^u, c^u)$ is the hyperprior distribution for independent flux $\boldsymbol{u}$, $p(\varepsilon)$ is the prior distribution for elasticity coefficients ε, $p(\boldsymbol{\beta})$ is the prior distribution for mRNA-to-protein ratios $\boldsymbol{\beta}$, $p(\widehat{\sigma^e})$ is the prior distribution for parameter of error term σ^e, and $p(\widehat{\sigma^t})$ is the prior distribution for parameter of error term σ^t.

Application of OMELET to mouse data

We applied OMELET to the experimental data from mice in four conditions: WT in the fasting state, WT after oral glucose administration, *ob*/*ob* in the fasting state, and *ob*/*ob* after oral glucose administration. The independent fluxes were constrained so that the flux through G6PC in WT mice in the fasting state was fixed at one. A metabolic flux through each reaction was inferred simultaneously in all the conditions and as inferred as the relative value to that through G6PC in WT mice in the fasting state. The amounts of pyruvate and oxaloacetate were not available in our measurements because of their chemical instability and low concentrations. For such metabolite species, the relative amounts normalized to the mean across the conditions were inferred as parameters. The amounts of enzymes of glutamic pyruvic transaminase (Gpt) and glutamate dehydrogenase 1 (Glud1) were not measured and only the likelihood of the measured amounts of transcripts was evaluated. Several enzymes function as complex including succinate dehydrogenase, which is also known as respiratory complex II. Two subunits of succinate dehydrogenase, subunit A (Sdha) and subunit B (Sdhb), were available both in the amounts of enzymes and transcripts. The amounts of Sdha and Sdhb were independently normalized to the mean values across the conditions, and then the product was introduced as $\boldsymbol{e}$ for the reaction through succinate dehydrogenase (SDH) in (Equation 10). Other reactions were catalyzed by a single enzyme or by complex with only one subunit measured and a single enzyme data was used. The parameters for coefficient of variances c^u and $c^{\dot{x}}$ were fixed at 0.1 and 0.01, respectively.

We performed posterior predictive checks to evaluate the fitting of the model to the measured data of the amounts of enzymes and transcripts from mice. Posterior predictive distributions of enzymes can be simulated by sampling parameters from the posterior and using them to generate replicate data sets based on (Equation 10). Posterior predictive distributions of transcripts can be simulated in the same way based on (Equation 13). We compared the posterior predictive distributions with the measured data and confirmed the good fits to the experimental data of the amounts of enzymes and transcripts (Figure S5).

Parameter estimation

Based on the specified prior distribution and likelihood, the posterior distributions of parameters were numerically estimated by Markov Chain Monte Carlo (MCMC) sampling. The algorithm was a No-U-turn sampler (NUTS), a variant of Hamiltonian Monte Carlo (HMC), constructing an iterative process that eventually converges to the true posterior distribution (Hoffman and Gelman, 2014). For application to the data from mice, we ran four chains of 20,000 iterations with 10,000 burnings with thinning of 2, resulting in 20,000 samples in total. Convergence of Markov Chains was evaluated by R-hat diagnostic, which compares the between- and within-chain estimated for model parameters. All our runs satisfied R-hat less than 1.05, indicating that chains were mixed well. All the parameter estimation was performed using RStan library (version 2.19.2) in R software (3.6.1) within a Docker container (Merkel, 2014).

Simulation using hepatocyte kinetic model

The model of hepatocyte glucose metabolism (Marín-Hernández et al., 2020) was kindly provided by Dr. Álvaro Marín Hernández and Dr. Emma Saavedra as COPASI (Complex Pathway Simulator) format (Hoops et al., 2006). The kinetic model represented the glycolytic pathway from glucose down to lactate as well as the pentose phosphate pathway and glycogen metabolism. We used the reactions except for cofactor metabolism (NADPH consumption, ATP-consuming processes, adenylate kinase, nucleotide diphosphate kinase, glutathione reductase, and glutathione peroxidase) because the mass balance for cofactors is not considered in OMELET. We also excluded transketolase reaction because of the fixed amounts of its

substrates, which makes it difficult to infer metabolic flux through transketolase using the relative amounts of metabolites across conditions in OMELET. Briefly, we first perturbed the original model (WT) to generate models of four mutant strains (mutant 01 to 04), and then 50 datasets including the amounts of metabolites, enzymes, and metabolic fluxes were generated for each of the models. The parameters of the WT model in enzyme i (z_i^0) to be perturbed included rate constants of mass action, Vmax for forward and backward, or constant fluxes. The magnitude of perturbation ζ_l (l = 1,…,5), strain-specific noise, was set so that mutant strains with perturbed parameter sets z^l were gradually deviated from the WT model (Table S8).

Based on the perturbed model, sample datasets were generated by introducing sample-specific noises $\zeta_i^{\text{sample}} \sim \mathcal{N}(0, (0.1z_i^l)^2)$ for each parameter value z_i^l, which represented variety between samples in the same strain and were assumed to be common in all the strains. Steady-state simulation using the parameter set with the strain-specific and sample-specific noises produced a dataset containing 50 samples with the amounts of metabolites, enzymes, and metabolic fluxes under each of the five conditions. The perturbed parameter names and values in the hepatocyte kinetic model are listed in Table S4. All the steady-state simulation were executed using COPASI software (Hoops et al., 2006).

To evaluate the performance of OMELET, only the dataset of the amounts of enzymes and metabolites, not including metabolic fluxes, were used as input. Since the amounts of transcripts were not available, we obtained the joint posterior distribution

$$p(\boldsymbol{v}, \varepsilon, \boldsymbol{\beta}, \widehat{\sigma^e} | \boldsymbol{e}, \boldsymbol{x}, c^u, c^{\dot{x}}, S) \propto p(\boldsymbol{e}|\boldsymbol{x}, \boldsymbol{v}, \varepsilon, \widehat{\sigma^e}) p(\boldsymbol{v}|\boldsymbol{u}, c^{\dot{x}}, S) p(\boldsymbol{u}|\boldsymbol{\mu}^u, c^u) p(\varepsilon) p(\boldsymbol{\beta}) p(\widehat{\sigma^e}) \quad \text{(Equation 16)}$$

where the likelihood of transcripts (Table S6) was removed from (Equation 15). The independent fluxes were constrained so that the metabolic flux through glucose uptake (glucose transporter; GLUT) in WT strain was fixed at one. A metabolic flux through each reaction was inferred as the relative value to that through GLUT in WT. The parameters for coefficient of variances c^u and $c^{\dot{x}}$ were fixed at 0.1 and 0.01, respectively. For MCMC sampling, we ran four chains of 5,000 iterations with 2,500 burnings with thinning 2, resulting in 5,000 samples in total. The metabolic fluxes inferred by OMELET were then compared with those obtained from the perturbation and steady-state simulation of the kinetic model.

Simulation using yeast kinetic model

The model of yeast glycolysis was downloaded from the public model repository BioModels Database (Le Novère et al., 2006) as SBML (Systems Biology Markup Language) format (Hucka et al., 2003), with the identifier BIOMD0000000503 (Messiha et al., 2014; Smallbone et al., 2013). The kinetic model represented the glycolytic pathway from glucose down to ethanol as well as the pentose phosphate pathway, and only the glycolytic part was used in our simulation. Briefly, we first perturbed the original model (WT) to generate models of four mutant strains (mutant 01 to 04), and then 50 datasets including the amounts of metabolites, enzymes, and metabolic fluxes were generated for each of the models. The parameters of the WT model in enzyme i (z_i^0) to be perturbed included kcat, Vmax, or an enzyme concentration. The magnitude of perturbation ζ_l (l = 1,…,5), strain-specific noise, was set so that mutant strains with perturbed parameter sets $\boldsymbol{z}^l$ were gradually deviated from the WT model (Table S8).

Based on the perturbed model, sample datasets were generated by introducing sample-specific noises $\zeta_i^{\text{sample}} \sim \mathcal{N}(0, (0.1z_i^l)^2)$ for each parameter value z_i^l, which represented variety between samples in the same strain and were assumed to be common in all the strains. Steady-state simulation using the parameter set with the strain-specific and sample-specific noises produced a dataset containing 50 samples with the amounts of metabolites, enzymes, and metabolic fluxes under each of the five conditions. The perturbed parameter names and values in the yeast kinetic model are listed in Table S4. All the steady-state simulation were executed using the Simbiology toolbox in MATLAB (The MathWorks, Inc., Natick, Massachusetts, United States of America).

To evaluate the performance of OMELET, only the dataset of the amounts of enzymes and metabolites, not including metabolic fluxes, were used as input. We obtained the joint posterior distribution described in (Equation 16). The independent fluxes were constrained so that the metabolic flux through glucose uptake (hexose transporter; HXT) in WT strain was fixed at one. A metabolic flux through each reaction was inferred as the relative value to that through HXT in WT. The parameters for coefficient of variances c^u and $c^{\dot{x}}$ were fixed at 0.1 and 0.01, respectively. For MCMC sampling, we ran four chains of 20,000 iterations with 17,500 burnings with thinning 2, resulting in 5,000 samples in total. The metabolic fluxes inferred by OMELET were

then compared with those obtained from the perturbation and steady-state simulation of the kinetic model.

Contributions of regulators to flux changes

We define a contribution ψ_{jh} of regulator h to changes in metabolic flux through reaction j between conditions. The regulators include transcripts, unaccounted enzyme regulators, substrates, products, cofactors, allosteric effectors, and unaccounted flux regulators. The unaccounted enzyme regulators can include other regulatory mechanisms of the protein amount of enzyme such as protein degradation and stability. The unaccounted flux regulators can include other regulators such as phosphorylation of enzymes and unknown allosteric effectors not included in OMELET. The concept of the contribution is to partition the cause of changes in metabolic flux between conditions into underlying changes in the amounts of regulators including enzymes and metabolites. The contribution was calculated based on propagation of uncertainty of regulators' amounts to metabolic flux, and a similar approach was described in a previous study (Hackett et al., 2016). Note that we analyzed only the local effects of regulators on changes in metabolic flux and do not evaluate the effects on changes in metabolic flux in which the regulator was not directly participated.

Before we calculated the contribution, we define the amounts of unaccounted flux regulators and unaccounted enzyme regulators. Based on (Equation 9), the inferred metabolic flux through reaction j in condition l can be described as

$$v_{jl} = \widehat{v}_{jkl} + \varphi^{v}_{jkl} = v^{0}_{j} e_{jkl}\left(1 + \varepsilon_{j}^{\top} \ln \mathbf{x}_{kl}\right) + \varphi^{v}_{jkl}. \quad \text{(Equation 17)}$$

φ^{v}_{jkl} is the amount of an unaccounted flux regulator in sample k in condition l and represents the deviation of the inferred metabolic flux from that calculated using linlog kinetics. Similarly, based on (Equation 13), the measured amount of enzyme in reaction j can be described as

$$e_{jkl} = \beta_{jl} t_{jkl} + \varphi^{e}_{jkl}. \quad \text{(Equation 18)}$$

φ^{e}_{jkl} is the amount of an unaccounted enzyme regulator and represents the deviation of the measured amount of the enzyme from that calculated using the amount of transcript and the mRNA-to-protein ratio. Combining (Equations 17 and 18), we obtain

$$v_{jl} = v^{0}_{j}\left(\beta_{jl} t_{jkl} + \varphi^{e}_{jkl}\right)\left(1 + \varepsilon_{j}^{\top} \ln \mathbf{x}_{kl}\right) + \varphi^{v}_{jkl} \quad \text{(Equation 19)}$$

which represents metabolic flux v_{jl} as a function of the transcript t_{jkl}, the unaccounted enzyme regulator φ^{e}_{jkl}, the metabolites $\mathbf{x}_{kl}$ including substrates, products, cofactors and allosteric effectors, as well as the unaccounted flux regulator φ^{v}_{jkl}.

We defined the contribution to changes in metabolic flux from transcripts, unaccounted enzyme regulators, and metabolites of substrates, products, cofactors, and allosteric effectors, as well as unaccounted flux regulators. Based on propagation of uncertainty, assuming that interactions between regulators is ignored, the variance $\mathrm{Var}(v_j)$ of inferred metabolic flux v_j through reaction j can be approximated as

$$\mathrm{Var}(v_j) \approx \sum_{h}\left(\frac{\partial v_j}{\partial y_{jh}}\right)^{2} \mathrm{Var}\left(y_{jh}\right) \quad \text{(Equation 20)}$$

with the amount of regulator h (y_{jh}), the sensitivity of the metabolic flux to the regulator $\partial v_j/\partial y_{jh}$, and the variance of the amount of the regulator $\mathrm{Var}(y_{jh})$. Regulator h is the transcript, the unaccounted enzyme regulator, substrate, product, cofactor, allosteric effector, or unaccounted flux regulator. The variance of the amount of the regulator between two conditions $\mathrm{Var}(y_{jh})$ is expressed as the change in the amount of the regulator between the two conditions Δy_{jh} as

$$\mathrm{Var}\left(y_{jh}\right) = \left(\frac{\Delta y_{jh}}{2}\right)^{2}. \quad \text{(Equation 21)}$$

The sensitivity of the metabolic flux to each regulator $\partial v_j/\partial y_{jh}$ is defined based on (Equations 17 and 19) as

$$\frac{\partial v_j}{\partial y_{jh}} = \begin{cases} \overline{\beta_j} v_j^0 \left(1 + \varepsilon_j^{\top} \ln \overline{\mathbf{x}}\right) & \text{if regulator } h \text{ is the transcript} \\ v_j^0 \left(1 + \varepsilon_j^{\top} \ln \overline{\mathbf{x}}\right) & \text{if regulator } h \text{ is the unaccounted enzyme regulator} \\ \dfrac{v_j^0 \overline{e_j} \varepsilon_{ji}}{\overline{y_{jh}}} & \text{if regulator } h \text{ is a metabolite} \\ 1 & \text{if regulator } h \text{ is the unaccounted flux regulator} \end{cases}, \quad \text{(Equation 22)}$$

where $\overline{\mathbf{x}}$ and $\overline{e_j}$ indicate the means of the metabolites and enzyme in reaction j across two conditions, respectively. Using the variance and the sensitivity of the metabolic flux to the amount of each regulator, we defined a contribution of the change in regulator h to the change in metabolic flux through reaction j as

$$\psi_{jh} = \frac{\left(\frac{\partial v_j}{\partial y_{jh}}\right)^2 \left(\Delta y_{jh}\right)^2}{\sum_h \left(\frac{\partial v_j}{\partial y_{jh}}\right)^2 \left(\Delta y_{jh}\right)^2}. \quad \text{(Equation 23)}$$

The contribution was a compositional data whose sum of the contributions of all the regulators to a change in metabolic flux equals one. The contribution ranged from zero to one, and the larger value meant the stronger effect of the regulator to the change in metabolic flux.

The contribution was calculated for changes in metabolic flux through each reaction between each pair of condition (Figure S8); WT and *ob*/*ob* mice in the fasting state, WT and *ob*/*ob* mice after oral glucose administration, fasting and after oral glucose administration in WT mice, and fasting and after oral glucose administration in *ob*/*ob* mice. Therefore, the calculated contributions represent the extent to which a change in each regulator contributed to the change in metabolic flux between the conditions.

Metabolomic analysis

Metabolomic measurements were performed as previously described (Egami et al., 2021; Kokaji et al., 2020). Total metabolites and proteins were extracted from the liver with methanol:chloroform:water (2.5:2.5:1) extraction. Approximately 40 mg of the liver was suspended with 500 μL of ice-cold methanol containing internal standards [20 μM L-methionine sulfone (Wako), 2-morpholinoethanesulfonic acid (Dojindo), and D-Camphor-10-sulfonic acid (Wako)] for quantification of metabolites, then with 500 μL of chloroform, and finally with 200 μL of water. After centrifugation at 4,600 × g for 15 min at 4 °C, the separated aqueous layer was filtered through a 5 kDa cutoff filter (Human Metabolome Technologies) to remove protein contamination. The filtrate (320 μL) was lyophilized and, prior to MS analysis, dissolved in 50 μL water containing reference compounds [200 μM each of trimesic acid (Wako) and 3-aminopyrrolidine (Sigma-Aldrich)]. Proteins were precipitated by addition of 800 μL of ice-cold methanol to the interphase and organic layers and centrifuged at 12,000 × g for 15 min at 4 °C. The pellet was washed with 1 mL of ice-cold 80% (v/v) methanol and resuspended in 1 mL of sample buffer containing 1% SDS and 50 mM Tris-Cl pH8.8, followed by sonication. The total protein concentration was determined by bicinchoninic acid (BCA) assay and was used for normalization of metabolite concentration among samples.

All CE-MS experiments were performed using an Agilent 1600 Capillary Electrophoresis system (Agilent technologies), an Agilent 6230 TOF LC/MS system, an Agilent 1200 series isocratic pump, a G1603A Agilent CE-MS adapter kit, and a G1607A Agilent CE electrospray ionization (ESI)-MS sprayer kit. Briefly, to analyze cationic compounds, a fused silica capillary [50 μm internal diameter (i.d.) × 100 cm] was used with 1 M formic acid as the electrolyte (Soga and Heiger, 2000). Methanol/water (50% v/v) containing 0.01 μM hexakis(2,2-difluoroethoxy)phosphazene was delivered as the sheath liquid at 10 μL/min. ESI-TOFMS was performed in positive ion mode, and the capillary voltage was set to 4 kV. Automatic recalibration of each acquired spectrum was achieved using the masses of the reference standards ([^{13}C isotopic ion of a protonated methanol dimer ($2CH_3OH+H$)]$^+$, *m/z* 66.0631) and ([hexakis(2,2-difluoroethoxy)phosphazene +H]$^+$, *m/z* 622.0290). The metabolites were identified by comparing their m/z values and relative migration times to the metabolite standards. Quantification was performed by comparing peak areas to calibration curves generated using internal standardization techniques with methionine sulfone. The other conditions were identical to those described previously (Soga et al., 2006). To analyze anionic metabolites, a commercially

available COSMO(+) (chemically coated with cationic polymer) capillary (50 μm i.d. × 105 cm) (Nacalai Tesque, Kyoto, Japan) was used with a 50 mM ammonium acetate solution (pH 8.5) as the electrolyte. Methanol/5 mM ammonium acetate (50% v/v) containing 0.01 μM hexakis(2,2-difluoroethoxy)phosphazene was delivered as the sheath liquid at 10 μL/min. ESI-TOFMS was performed in negative ion mode, and the capillary voltage was set to 3.5 kV. Automatic recalibration of each acquired spectrum was achieved using the masses of the reference standards ([^{13}C isotopic ion of a deprotonated acetate dimer ($2CH_3COOH-H$)]$^-$, *m/z* 120.0384) and ([hexakis(2,2-difluoroethoxy)phosphazene +deprotonated acetate ($CH_3COOH-H$)]$^-$, *m/z* 680.0355). For anion analysis, D-camphor-10-sulfonic acid were used as the internal standards. The other conditions were identical to those described previously (Soga et al., 2009). The acquired raw data were analyzed using our proprietary software (Sugimoto et al., 2010).

Proteomic analysis

Sample preparation of proteomic analysis. Sample preparation of proteome analysis were performed as described, previously (Matsumoto et al., 2017). Frozen powder of liver and muscle were lysed with a solution containing 2% SDS, 7 M urea, and 100 mM Tris-HCl, pH 8.8, and then subjected to ultrasonic treatment (five times for 30 s with intervals of 30 s) with a Bioruptor (Diagenode). The samples were diluted with an equal volume of water. The protein concentrations of the samples were determined with BCA assays (Bio-Rad), after which portions (200 μg of protein) were subjected to methanol–chloroform precipitation. The resulting pellet was dissolved in digestion buffer (0.5 M triethylammonium bicarbonate containing 7 M guanidine hydroxide) and heated at 56°C for 30 min. Each sample was diluted with an equal volume of water, after which portions were subjected to BCA assays. The remaining solution (50 μl) was diluted with 50 μl of water and subjected to digestion with lysyl-endopeptidase (2 μg, Wako) for 4 h at 37°C. After the addition of 100 μl of water, the samples were further digested with trypsin (2 μg, Thermo Fisher) for 14 h at 37°C. To block cysteine/cystine residues, we treated the digest with 0.625 mM Tris(2-carboxyethyl)phosphine hydrochloride (Thermo Fisher) for 30 min at 37°C, then performed alkylation with 3.125 mM 2-iodoacetoamide (Sigma) for 30 min at room temperature and quenching with 2.5 mM N-acetyl-l-cysteine (Sigma). The resulting digests were freeze-dried and then labeled with the mTRAQΔ0 reagent (SCIEX). For a deep proteomics, tryptic digests were separated into 6 fractions with off-Line high-pH reverse phase chromatography (Matsumoto et al., 2017).

DDA of peptides for multiple reaction monitoring (MRM) method development. Target proteins were selected from the proteins listed in three Kyoto Encyclopedia of Genes and Genomes (KEGG) pathways; Glycolysis / Gluconeogenesis (mmu00010), Citrate cycle (mmu 00020), and Starch and sucrose metabolism (mmu 00500), and proteins related to insulin signaling. A key step for the establishment of a successful targeted proteomic analysis is the accurate selection of proteotypic peptides (PTPs) for the targets of interest. Therefore, we first performed a discovery phase aimed at the selection of PTPs, which was based on a deep proteomic characterization of total protein extract of the murine liver and muscle. mTRAQ-labeled peptides as mentioned above were fractionated by reversed-phase chromatography on a 16-cm column (inner diameter, 100 μm) packed in house with 2-μm L-column C18 material (CERI). Peptides were eluted with a linear gradient (typically 5–45% B for 40 min, 45–95% B for 1 min, and 95% B for 10 min, where A was 0.1% formic acid and 2% acetonitrile, and B was 0.1% formic acid and 90% acetonitrile), at a flow rate of 200 nl/min. The high-performance LC system (Eksigent nano-LC) was coupled to a TripleTOF5600 hybrid mass spectrometer (SCIEX). Data acquisition was performed in IDA mode with the iTRAQ option. Survey MS spectra were acquired for 100 ms, and the 10 most intense ions were isolated and then fragmented with an automatically optimized collision energy for an MS/MS acquisition time of 100 ms. Peak lists (mgf) generated by the AB SCIEX MS Data Converter were used to search a database containing IPI mouse version 3.44 (55 078 protein entries; IPI, European Bioinformatics Institute) protein sequences concatenated with decoy sequences, with the use of the MASCOT algorithm (Matrix Science). The search was conducted with the following parameter settings: trypsin was selected as the enzyme used, the allowed number of missed cleavages was set to two, and the mTRAQΔ0 label on the NH2-terminal or lysine residues and carbamidomethylation of cysteine were selected as fixed modifications. Oxidized methionine and the mTRAQΔ0 label on tyrosine were searched as variable modifications. The precursor mass tolerance was 50 p.p.m., and the tolerance of MS/MS ions was 0.02 mass/charge (m/z) units. We imported all significant peptide-spectrum matches (PSMs) (MASCOT score >20) into a relational database written in MySQL. From this dataset, we preferentially selected PTP candidates which met the following criteria: 1. more than six amino acids; 2. absence of tryptic missed-cleavage sites; 3. The C-terminus of PTPs is Lys or Arg; 4. absence of

Please cite this article in press as: Uematsu et al., Multi-omics-based label-free metabolic flux inference reveals obesity-associated dysregulatory mechanisms in liver glucose metabolism, iScience (2022), https://doi.org/10.1016/j.isci.2022.103787

methionine residues. To verify whether these PTP candidates were actually identified and quantified in our MRM systems, trypsin digests used in "DDA of peptides for MRM method development" were labeled with either mTRAQΔ0 or mTRAQΔ4 and subjected to MRM assays. All MRM traces were analyzed by iMPAQT-quant (Matsumoto et al., 2017). Peak groups were scored on the basis of cosine similarity with MS/MS spectra obtained in DDA, peak coelution of at least three fragment ions for each peptide, the presence or absence of interfering ions, and intensity. Finally, we selected 2-3 PTPs per target protein and purchased from Funakoshi Co. All PTPs were resuspended with 20%-50% ethanol, pooled and labeled with mTRAQΔ4 using standard procedures.

MRM analysis. MRM analysis was performed with a QTRAP5500 instrument (SCIEX) equipped with nano-Advance UHPLC (MICHROM) and HTS-PAL/xt autosampler (CTC Analytics AG). Peptides were eluted with a linear gradient of 5%–30% B for 45 min, 30%–95% B for 46 min (where A is 0.1% formic acid and B is acetonitrile) at a flow rate of 200 nL/min. Parameters were set as follows: spray voltage, 2,000 V; curtain gas setting, 10; collision gas setting, high; ion-source gas-1 setting, 30 and interface-heater temperature, 150°C. Collision energy (CE) was calculated with the following formulae: CE = (0.044 × m/z1) + 5.5 and CE = (0.051 × m/z1) + 0.5 (where m/z1 is the m/z of the precursor ion) for doubly and triply charged precursor ions, respectively. Collision-cell exit potential (CXP) was calculated according to the formula: CXP = (0.0391 × m/z2) − 2.2334 (where m/z2 is the m/z of the fragment ion). The declustering potential (DP) was set to 50, and the entrance potential (EP) was set to 10. Resolution for Q1 and Q3 was set to 'unit' (half-maximal peak width of 0.7 m/z). The scheduled MRM option was used for all data acquisition, with a target scan time of 2.0 s and MRM detection windows of 300s. More than three technical repeats were performed per sample. Raw data were analyzed by iMPAQT-Quant (Matsumoto et al., 2017) with the corresponding spectra library. Peak groups were scored on the basis of cosine similarity with the MS/MS spectra obtained in DDA, a peak co-elution of at least three fragment ions for each peptide, the presence or absence of interfering ions, and the intensity. Finally, all traces were manually checked to eliminate inadequate transitions. All quantified transitions were normalized across samples and converted into protein abundance by SRMstats software on R (Surinova et al., 2013).

Transcriptomic analysis

Transcriptomic measurements were performed as previously described (Egami et al., 2021; Kokaji et al., 2020). Briefly, total RNA was extracted from the liver using RNeasy Mini Kit (QIAGEN) and QIAshredder (QIAGEN) and assessed for quantity using Nanodrop (Thermo Fisher Scientific) and for quality using the 2100 Bioanalyzer (Agilent Technologies). cDNA libraries were prepared using SureSelect strand-specific RNA library preparation kit (Agilent Technologies). The resulting cDNAs were subjected to 100-bp paired-end sequencing on an Illumina HiSeq2500 Platform (Illumina) (Matsumoto et al., 2007). Sequences were aligned to the mouse reference genome obtained from Ensembl database (Cunningham et al., 2015; Flicek et al., 2014) (GRCm38/mm10, Ensembl release 70) using the software package TopHat (Trapnell et al., 2009, 2012) (v.2.0.9), software in the Tuxedo tool. Cufflinks (v.2.2.1), software in the Tuxedo tool, was used to assemble transcript models from aligned sequences and to estimate the number of transcripts as an indicator of gene expression. The number of transcripts was shown as fragments per kilo base of exon per million mapped fragments.

Blood glucose and insulin

The blood and insulin data at 0, 2, 5, 10, 15, 20, 30, 45, 60, 90, 120, 180, 240 minutes after oral glucose administration were previously reported (Kokaji et al., 2020).

QUANTIFICATION AND STATISTICAL ANALYSIS

For the metabolites, enzymes, and transcripts, we defined increased and decreased molecules between the conditions using the following procedure (Figure 2; Table S2). For each molecule, we calculated the fold change of the mean amount of WT mice in the fasting state, WT mice after oral glucose administration, *ob/ob* mice in the fasting state, and *ob/ob* mice after oral glucose administration over the mean amount of WT mice in the fasting state. The significance of changes was tested by two-tailed Welch's t-test for each molecule. The q values were calculated by Benjamini-Hochberg procedure. Molecules that showed an q value less than 0.05 are defined as significantly changed molecules. Among them, molecules with a fold change larger than 1.5 were defined as increased molecules between the conditions, whereas molecules

with a fold change smaller than 0.67 were defined as decreased molecules. The Pearson correlation coefficient was calculated between the medians of fold changes of metabolic fluxes of mutants over those of WT inferred by OMELET and the means of those simulated by the kinetic models across all the reactions (Figures S2D and S2E). The Pearson correlation coefficient was calculated between the medians of metabolic fluxes inferred by OMELET and the means of metabolic fluxes in the previous studies across all the reactions in all the conditions (Figures S6B and S6D). The p-value was computed by transforming the correlation to create a t statistic having N-2 degree of freedom, where N is the number of samples.